Origin of long lifetime of band-edge charge carriers in organic–inorganic lead iodide perovskites

Tianran Chen[a,1], Wei-Liang Chen[b,1], Benjamin J. Foley[c], Jooseop Lee[d], Jacob P. C. Ruff[d], J. Y. Peter Ko[d], Craig M. Brown[e], Leland W. Harriger[e], Depei Zhang[a], Changwon Park[f], Mina Yoon[f], Yu-Ming Chang[b], Joshua J. Choi[c,2], and Seung-Hun Lee[a,2]

[a]Department of Physics, University of Virginia, Charlottesville, VA 22904; [b]Center for Condensed Matter Sciences, National Taiwan University, Taipei 10617, Taiwan; [c]Department of Chemical Engineering, University of Virginia, Charlottesville, VA 22904; [d]Cornell High Energy Synchrotron Source, Cornell University, Ithaca, NY 14853; [e]NIST Center for Neutron Research, National Institute of Standards and Technology, Gaithersburg, MD 20899; and [f]Center for Nanophase Materials Sciences, Oak Ridge National Laboratory, Oak Ridge, TN 37831

Long carrier lifetime is what makes hybrid organic–inorganic perovskites high-performance photovoltaic materials. Several microscopic mechanisms behind the unusually long carrier lifetime have been proposed, such as formation of large polarons, Rashba effect, ferroelectric domains, and photon recycling. Here, we show that the screening of band-edge charge carriers by rotation of organic cation molecules can be a major contribution to the prolonged carrier lifetime. Our results reveal that the band-edge carrier lifetime increases when the system enters from a phase with lower rotational entropy to another phase with higher entropy. These results imply that the recombination of the photoexcited electrons and holes is suppressed by the screening, leading to the formation of polarons and thereby extending the lifetime. Thus, searching for organic–inorganic perovskites with high rotational entropy over a wide range of temperature may be a key to achieve superior solar cell performance.

organic–inorganic hybrid perovskite | carrier lifetime | photoluminescence | polaron

The record efficiency of hybrid organic–inorganic perovskite (HOIP)-based solar cells has reached above 22% (1–4), which is comparable to that of silicon solar cells. The most dominant contribution to the high photovoltaic performance of HOIPs comes from their long carrier lifetimes (≥ 1 µs), which translates to large carrier diffusion lengths despite their modest charge mobilities (5). Several microscopic mechanisms behind the unusually long carrier lifetime have been proposed, such as formation of ferroelectric domains (6–9), Rashba effect (10–12), photon recycling (13), and large polarons (14–16). When the HOIPs are replaced with all inorganic perovskites in the solar cell architecture, the device can still function as a solar cell. This indicates that the photons excite electrons and holes out of the inorganic metal halide atoms, which is consistent with the density functional theory (DFT) calculations that the corner interstitial cations, whether organic or inorganic, do not directly contribute to the band-edge states (17). However, the efficiency of the purely inorganic perovskites is currently at ~11% (18–20), which is far below 22% of HOIP-based solar cells. This suggests that the presence of organic cation may be the key for achieving high solar cell efficiency. It is, however, yet to be understood how the organic cations enhance the efficiency.

Among the aforementioned microscopic mechanisms, three are based on the role of organic cations. First, in the ferroelectric domain theory, nanoscale ferroelectric domains are formed due to alignment of organic cations (6–9). Such domains can spatially separate the photoexcited electron and holes and thereby reduce their recombination. Second, in the Rashba effect theory (10–12), the spin and orbit degrees of freedom of the inorganic atoms are coupled with the electric field generated by the organic cations. This results in the electronic band splitting for different spins and leads to an effectively indirect band gap and the prolonged lifetime.

Third, it was proposed that large polarons are formed by organic cations when they reorient themselves in response to the presence of photoexcited electrons and holes (14–16). As a result, the screened carriers are protected from scattering by defects and phonons, leading to the prolonged lifetime. Testing these theories calls for experimental studies on microscopic correlations between the motion of organic cations and the charge carrier lifetime. An experimental challenge is how to directly correlate the relaxation of band-edge carriers and intrinsic properties at the atomic level, without complications with extrinsic factors such as morphology and charge trap density across different samples.

Here, the intrinsic effects of organic molecules on the band-edge charge carrier lifetime were studied by probing band-edge time-resolved photoluminescence (TRPL) of HOIPs as a function of temperature, spanning different structural phases of each system with different rotational entropy. Among HOIPs with various organic cations, we have selected two prototypes for this study: formamidinium lead iodide [$HC(NH_2)_2PbI_3$] and methylammonium lead iodide ($CH_3NH_3PbI_3$). The primary reason of the choice is that the $HC(NH_2)_2^+$ and $CH_3NH_3^+$ molecules have different geometries: the ~120° bent and the linear geometry of the C–N bonds in $HC(NH_2)_2^+$ and $CH_3NH_3^+$, respectively. As a consequence, $CH_3NH_3^+$ has a strong electric dipole moment (6), whereas $HC(NH_2)_2^+$ has a strong quadrupole moment that has not been considered before.

Significance

Hybrid organic–inorganic perovskites (HOIPs) are among the most promising materials for next-generation solar cells that combine high efficiency and low cost. The record efficiency of HOIP-based solar cells has reached above 22%, which is comparable to that of silicon solar cells. HOIP solar cells can be manufactured using simple solution processing methods that can be drastically cheaper than the current commercial solar cell technologies. Despite the progress so far, the microscopic mechanism for the high solar cell efficiency in HOIPs is yet to be understood. Our study shows that rotation of organic molecules in HOIPs extends the lifetime of photoexcited charge carriers, leading to the high efficiency. This insight can guide the progress toward improved solar cell performance.

APPLIED PHYSICAL SCIENCES

Furthermore, when caged in the environment of lead iodides, the molecules with different geometries will exhibit different characteristics of rotational motions and drive the HOIPs into different crystal structures. Upon cooling, $CH_3NH_3PbI_3$ undergoes successive cubic-to-tetragonal-to-orthorhombic transitions (21, 22). On the other hand, $HC(NH_2)_2PbI_3$ undergoes different structural-phase transitions depending on the cooling process (23); if cooled from room temperature, hexagonal structures are selected, whereas, if cooled from the high-temperature cubic phase, the hexagonal structures are entirely avoided. More importantly, the cubic phases of $CH_3NH_3PbI_3$ and $HC(NH_2)_2PbI_3$ have different molecular rotational entropy; in $CH_3NH_3PbI_3$ the $CH_3NH_3^+$ cation has preferential orientations (21, 22), whereas in $HC(NH_2)_2PbI_3$ the $HC(NH_2)_2^+$ cation has nonpreferential orientations (23), leading to a much higher rotational entropy for $HC(NH_2)_2PbI_3$ than for $CH_3NH_3PbI_3$. To study the intrinsic relation between the charge carrier lifetime and the rotational entropy of the molecule in HOIPs, we have systematically examined the charge carrier relaxation dynamics, crystal structures, and electronic band structures of the two HOIPs as a function of temperature spanning their structural phases, using time-averaged and time-resolved photoluminescence, neutron and X-ray scattering, and DFT analysis. We stress that, if any intrinsic correlation between the charge carrier relaxation and atomic properties of the system is present, it will manifest itself in the temperature dependences.

Our results revealed that the band-edge carrier lifetimes in both $HC(NH_2)_2PbI_3$ and $CH_3NH_3PbI_3$ increase when the systems enter from a structural phase with lower rotational entropy to another phase with higher entropy. For instance, the lifetime in $HC(NH_2)_2PbI_3$ dramatically changes from ~30 to ~300 ns as, upon heating, the system enters into its cubic phase with high rotational entropy. We stress that the sudden increase in the lifetime with increasing temperature cannot be accounted for by changes in defect density or electronic structure. One plausible scenario is that the photoexcited charge carriers are screened by reoriented organic cations, resulting in formation of large polarons that prolongs the charge carrier lifetime.

Temperature-History Dependent PL Spectra of $HC(NH_2)_2PbI_3$ and $CH_3NH_3PbI_3$

Photoluminescence (PL) measurements can directly probe the bandgap and charge recombination dynamics in HOIPs. Fig. 1 shows the time-integrated PL data, taken from a powder sample of $HC(NH_2)_2PbI_3$, upon heating, as a function of temperature from 80 to 440 K over a wide range of wavelength from 1.42 to 2.40 eV (see *SI Appendix* for the experimental details). Before each set of the measurements upon heating, the sample was initially cooled in two different conditions; in one case (Fig. 1 *A* and *B*), a fresh sample was cooled down to the base temperature from room temperature, that is, from the hexagonal phase (henceforth, we will call it HEAT1 process), and in the other case (Fig. 1 *C* and *D*), the sample was heated to 440 K and then quenched to the base temperature from the 440 K cubic phase (henceforth, we will call it HEAT2). After each cooling process, the PL data were collected, while heating to 440 K, at every 10 or 20 K. For $T > 400$ K, both cases exhibit the same emission peak centered at ~1.6 eV. For $T < 400$ K, however, they exhibit completely different PL spectra: most notably, when initially cooled from the room temperature hexagonal phase (HEAT1), the PL exhibits a broad emission peak centered at ~1.85 eV (Fig. 1 *A* and *B*). Surprisingly, when cooled from the cubic phase (HEAT2), the ~1.85-eV broad peak is completely absent at all temperatures and replaced with two sharper emission peaks at ~1.5 eV for $T < 300$ K (Fig. 1 *C* and *D*).

Note that, for the HEAT1 process, upon heating from 80 to 140 K, the ~1.85-eV emission peak experiences a blue shift of 0.08 eV, which is typical behavior due to the positive temperature coefficient of bandgap in lead halide perovskites (24). However, at 160 K, the
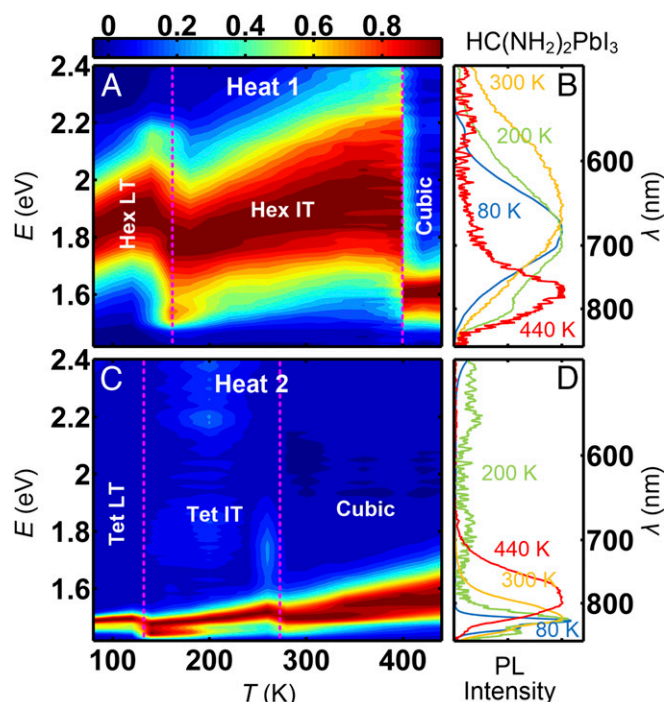

Fig. 1. Time-averaged photoluminescence (PL) spectra of $HC(NH_2)_2PbI_3$. (*A* and *B*) $HC(NH_2)_2PbI_3$ was first cooled from the room temperature Hex IT phase to the base temperature. Then, upon heating to 440 K (HEAT1), PL measurements were taken at 19 different temperatures. *A* shows a color contour map of the data, whereas *B* shows the PL data in 1D plot at four different temperatures: 80, 200, 300, and 440 K. (*C* and *D*) From 440 K, the sample was quenched to 77 K at a 30 K/min cooling rate. Then, similar PL measurements were performed, upon heating up to 440 K (HEAT2), at 19 different temperatures. *C* shows a color contour map of the data, whereas *D* shows the PL data in 1D plot at four different temperatures: 80, 200, 300, and 440 K. The vertical dotted lines in *A* and *C* represent the phase boundaries determined by neutron scattering (Fig. 3).

emission peak shifts back to 1.77 eV, and, upon further heating to 400 K, it experiences a blue shift of 0.14 eV. When the sample was held at 400 K for 45 min, the 1.91-eV emission peak disappeared, and instead the 1.6-eV emission peak appeared, which remained at higher temperatures. This indicates that, for HEAT1 process, there are three different phases separated at 160 (20) K and at 400 (10) K. For the HEAT2 process, the ~1.5-eV emission peaks exhibit similar reverse in the T-induced blue shift at 130 (10) K and at 270 (10) K. These indicate that, for each process, $HC(NH_2)_2PbI_3$ has three phases, although the nature of the phase transitions, such as the transition temperature and more starkly the bandgap, becomes different depending on the cooling history.

We have also performed time-averaged PL measurements on $CH_3NH_3PbI_3$ as a function of temperature. As shown in Fig. 2, over the measured temperature range from 80 to 400 K, the PL spectra exhibits sharp peaks at energies smaller than ~1.75 eV. No observable signal was detected for energies higher than 1.75 eV. This contrasts with $HC(NH_2)_2PbI_3$, which exhibits a broad peak centered at ~1.9 eV in its hexagonal phases, and is consistent with the fact that $CH_3NH_3PbI_3$ never transforms into a hexagonal system.

Structural Phase Transitions in $HC(NH_2)_2PbI_3$ and $CH_3NH_3PbI_3$

To understand the temperature dependence of the PL spectra of $HC(NH_2)_2PbI_3$, we have performed elastic neutron scattering measurements on the $HC(NH_2)_2PbI_3$ sample for the HEAT1 and HEAT2 processes. As shown in Fig. 3 *A* and *B*, for HEAT1, the system is in the low-temperature $P6_3/m$ hexagonal (Hex LT)
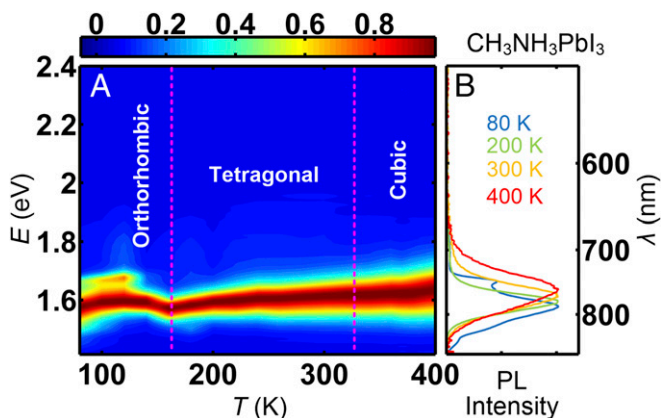
Fig. 2. Time-averaged PL spectra of $CH_3NH_3PbI_3$. *A* shows a color contour map of the data, whereas *B* shows the PL data in 1D plot at four different temperatures: 80, 200, 300, and 400 K.

phase (23) for $T < T_{Hex\ LT}^{HEAT1} = 180\ (5)$ K, and in the intermediate temperature $P6_3/mmc$ hexagonal (Hex IT) phase (23) for $T_{Hex\ LT}^{HEAT1} < T < T_{Cubic}^{HEAT1} = 400\ (20)$ K. Upon further heating, at T_{cubic}^{HEAT1} the system enters the high-temperature $Pm\bar{3}m$ cubic phase (23, 25). [See *SI Appendix* for comparison with previously reported results for deuterated $HC(ND_2)_2PbI_3$ (23).] The structural transition temperatures match closely with the phase boundaries determined by the PL data of HEAT1 (Fig. 1*A*), indicating that the change of PL spectra is intimately coupled with the structural-phase transitions.

For HEAT2, as shown in Fig. 3 *C* and *D*, at low temperatures [$T < T_{Cubic}^{HEAT2} = 280\ (5)$ K], the quenched phases of $HC(NH_2)_2PbI_3$ have very different crystal structures than the hexagonal structures, evidenced by the different Bragg peaks. We have performed neutron and synchrotron X-ray diffractions to determine the quenched structures to be tetragonal; the $P4bm$ tetragonal (Tet LT) for $T < T_{Tet\ LT}^{HEAT2} = 140\ (10)$ K and the $P4/mbm$ tetragonal (Tet IT) for $T_{Tet\ LT}^{HEAT2} < T < T_{Cubic}^{HEAT2}$. (See *SI Appendix* for the data and detailed refinement of the crystal structures for the tetragonal phases.) Upon further heating, for $T > T_{Cubic}^{HEAT2}$, the system becomes cubic. We note again that the structural-phase transition temperatures of HEAT2 by neutron scattering are also consistent with the transition temperatures observed in the PL measurements (Fig. 1*C*). Here, we show the Tet IT crystal structure in Fig. 4*C* that is mostly relevant to the discussion on the electronic band structure and charge carrier recombination. It is to be noted that, in the Tet IT phase, the organic molecules have strong preferential orientations as shown in Fig. 4*C*. This contrasts with the cubic phase in which the molecules have isotropic orientation with large entropy (23), as shown in Fig. 4*A*.

For $CH_3NH_3PbI_3$, we have performed elastic neutron scattering measurements to study the structural-phase transitions. *SI Appendix*, Fig. S3, shows that $CH_3NH_3PbI_3$ undergoes an orthorhombic-to-tetragonal phase transition at 164 (2) K, and a tetragonal-to-cubic phase transition at 325 (3) K, consistent with previous studies (22, 23).

First-Principles Electronic Structures of $HC(NH_2)_2PbI_3$ and $CH_3NH_3PbI_3$

To understand why the PL spectra change dramatically in different phases, we calculated electronic band structures for the determined crystal structures using DFT calculations (26–29). *SI Appendix*, Fig. S7, shows the calculated electronic band structures for the cubic, Hex IT, and quenched Tet IT phases of $FAPbI_3$. The band structures of Hex LT and Tet LT are similar to those of Hex IT and Tet IT, respectively, as shown in *SI Appendix*, Fig. S8. We

also performed the DFT calculations including the spin orbit coupling (SOC). Fig. 4 shows the resulting band structures for cubic, Hex IT, and Tet IT phases. It is known that the absolute bandgap values from DFT+SOC calculations are underestimated (30). However, the main focus here is to understand the evolution of the positions of the PL peaks through the structural-phase transitions, and we focus on relative changes in band structures rather than absolute values. Note that the cubic phase exhibits a weak static Rashba splitting at Γ point (0.01-eV splitting in the conduction band, which is negligible compared with thermal energy) due to the lack of inversion symmetry of the FA^+ molecule, and the Tet IT phase exhibits a weaker Rashba splitting at Z point. No such splitting was visible for the Hex IT phase.

In the calculated band structures shown in Fig. 4 and *SI Appendix*, Fig. S7, a few salient features should be noted; the cubic and quenched tetragonal phases have similar bandgaps that are much smaller than those of the hexagonal phases. Thus, the PL from band-edge charge carrier recombination will appear at lower energies in the cubic and tetragonal phases compared with the hexagonal phases. Indeed, this is consistent with our PL data (Fig. 1). Furthermore, the calculated band structures of the cubic and two quenched tetragonal phases have sharp cone-shape bands with direct bandgap with a negligible Rashba splitting. In contrast, the hexagonal phases have nearly flat valence band maximum (VBM) and conduction band minimum (CBM) with indirect bandgap. This is also consistent with the PL data that show the sharp emission peaks in the cubic and tetragonal phases compared with the broad emission peaks in the hexagonal phases. Considering the fast phonon-induced carrier relaxation time in comparison with the charge recombination time, carriers in hexagonal phase will be quickly thermalized to VBM and CBM. Therefore, the emission broadening of the hexagonal phase (Fig. 1*A*) is an indication of its enhanced electron–phonon scattering (31).
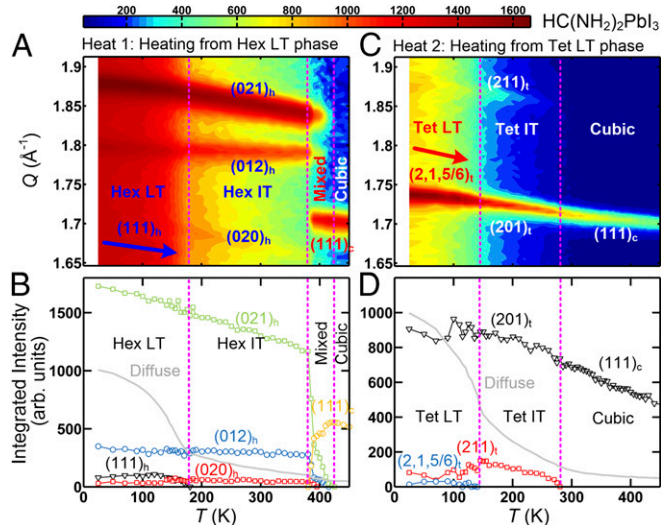

Fig. 3. Structural transitions of $HC(ND_2)_2PbI_3$. Elastic neutron scattering data obtained at the Spin-Polarized Inelastic Neutron Spectrometer, NIST Center for Neutron Research, for HEAT1 (*A* and *B*) and for HEAT2 (*C* and *D*) process. *A* and *C* are contour maps of the scattering intensity as a function of momentum transfer, Q, and temperature, T. Q range of 1.65 to 1.91 Å^{-1} was covered to probe the distinctive nuclear Bragg peaks; the $(111)_c$ peak associated with the cubic, $(020)_h$, $(012)_h$ and $(021)_h$ with Hex IT and Hex IT, $(111)_h$ with Hex LT, $(201)_t$ and $(211)_t$ with Tet IT and Tet LT, and the $(2,1,5/6)_t$ superlattice peak associated with Tet LT. *B* and *D* show the integrated intensities of the Bragg peaks as function of T. The light-gray line indicates the temperature-dependent diffuse scattering intensity that is due to freezing of the rotational motion of the organic molecule (21). The vertical dotted lines represent the phase boundaries.
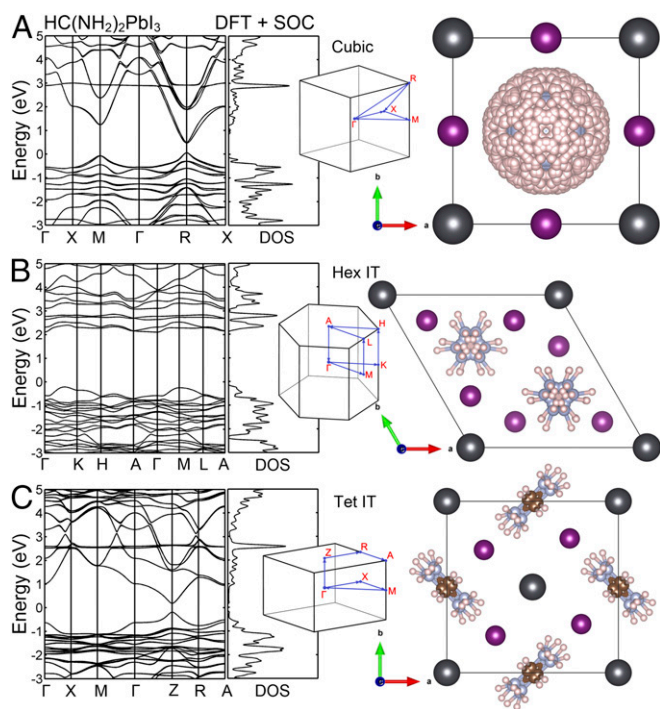
Fig. 4. Electronic band structure of $HC(NH_2)_2PbI_3$ for the cubic, Hex IT, and Tet IT phases. Electronic band structures were obtained by DFT calculations including SOC for the (A) cubic, (B) Hex IT, and (C) Tet IT phases. The crystal structures for the cubic and Hex IT phases were taken from ref. 21, whereas the crystal structure of the Tet IT phase was determined by Rietveld refinement of neutron diffraction and synchrotron X-ray data taken at 200 K. Here, all of the crystallographically equivalent positions of the FA^+ molecule are shown. The geometry of a single $HC(NH_2)_2^+$ molecule is shown in the *Inset* of Fig. 5F. Details of the refinements of Tet IT and Tet LT phases are described in *SI Appendix*.

For $CH_3NH_3PbI_3$, *SI Appendix*, Fig. S9, shows the calculated electronic band structures for the cubic, tetragonal, and orthorhombic phases. All phases show similar direct band gaps, which is consistent with their PL data shown in Fig. 2.

TRPL of $HC(NH_2)_2PbI_3$ and $CH_3NH_3PbI_3$

To probe dynamics of the charge recombination of the band-edge carriers in the different structural phases, we performed the TRPL measurements at the peak energy of the PL emission peak, that is, at the band edge, up to 1 μs. Fig. 5 shows TRPL data of HC $(NH_2)_2PbI_3$ for the HEAT1 and HEAT2 processes. We stress that all TRPLs were taken at the peak energy of the PL emission peaks (Fig. 1). To determine the PL lifetime, we fitted the TRPL data to a two-exponential reconvolution function as described in *SI Appendix*. Our analysis is aimed at comparing phenomenological lifetimes at a fixed excitation density across the phase transition boundaries. In HEAT1, the Hex LT phase ($T \lesssim 120$ K) exhibits an extremely long carrier lifetime, for instance, $\tau_{heat1}(80\ K) = 790\ (20)$ ns (black symbols in Fig. 5 A and C). This long lifetime of the band-edge charge carrier can be attributed to the fact that the recombination process is indirect in the hexagonal phase, as shown by our DFT calculations, and requires involvement of phonons. As T increases to 400 K, the lifetime of the band-edge charge carrier rapidly becomes shorter, for instance, $\tau_{heat1}(360\ K) = 1\ (1)$ ns, which is expected for phonon-assisted indirect recombination. Upon further heating and as the system enters the cubic phase, however, the lifetime increases dramatically: $\tau_{heat1}(440\ K) = 300(100)$ ns. This is a striking result, considering that the cubic phase has a direct bandgap that is supposed to yield a shorter lifetime than an indirect bandgap of the hexagonal phase. We argue that the higher degree

of rotational motions in the cubic phase that protect the band-edge charge carriers is responsible for the large enhancement of τ_{heat1} for the cubic phase. This is consistent with a recent study that revealed the transition to the cubic phase being driven by the enhancement of the rotational entropy of organic molecules (23).

In HEAT2, TRPL shows very different behaviors at low temperatures. $\tau_{heat2}(80\ K) = 39\ (6)$ ns of the Tet LT phase is much shorter than $\tau_{heat1}(80\ K) = 790\ (20)$ ns of the Hex LT phase. This is consistent with the bandgap in the tetragonal phases being direct, whereas the hexagonal phases have indirect bandgap. As T increases up to 240 K, τ_{heat2} of the tetragonal phases decreases as expected but much more slowly than observed in the hexagonal phases of HEAT1. The slower decrease rate of τ_{heat2} of the tetragonal phases is also consistent with the recombination process mainly being direct, thus less sensitive to phonon population. Upon further heating, τ_{heat2} abruptly increases as the system enters the cubic phase at ~280 K and remains nearly constant at ~260 ns. It is interesting that, in both HEAT1 and HEAT2 cases, the lifetime of charge carriers, τ_{heat1} and τ_{heat2}, suddenly increases when the system becomes cubic, regardless of the cooling history. The enhancement of τ_{heat1} can be explained by the completely different electronic band structure between the hexagonal and the cubic phase as shown in Fig. 4. However, the dramatic enhancement of τ_{heat2} in the cubic phase during the HEAT2 process is unusual because the electronic band structure of the tetragonal phase is similar to that of the cubic phase (Fig. 4 A and C).

Thus, regardless of what the lower temperature structure is, hexagonal in HEAT1 and tetragonal in HEAT2, the lifetime of the charge carriers dramatically increases as $HC(NH_2)_2PbI_3$ enters its cubic phase upon heating. We can rule out the change in defect density as the origin of the lifetime increase because the defect density is expected to increase with increasing temperature and thus decrease the charge carrier lifetime. We can also rule out the change in electronic structure as the origin because the hexagonal structure in HEAT1 has an indirect bandgap that is supposed to yield longer lifetime than the cubic phase with a direct bandgap, and the Tet IT structure in HEAT2 has a similar band structure as the cubic phase. A possible explanation of the unusual behavior of the lifetime comes from the fact that the organic molecules have strong preferential orientations in the hexagonal and tetragonal phases, whereas they have isotropic
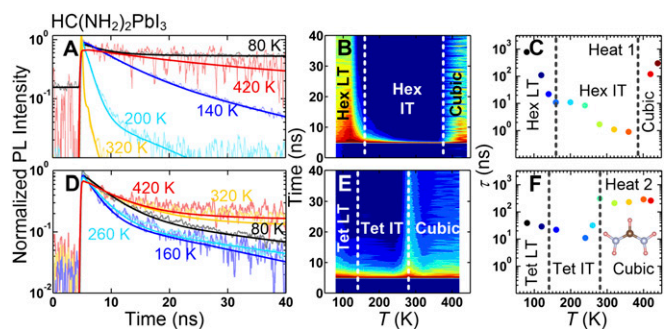

Fig. 5. Time-resolved photoluminescence (TRPL) spectra of $HC(NH_2)_2PbI_3$. (A and B) The TRPL spectra were taken at 11 different temperatures for HEAT1 process. A shows 1D plots of the spectra at 80, 140, 200, 320, and 420 K. B shows a color contour map of all 11-temperature data. (D and E) The TRPL spectra taken at 10 different temperatures for HEAT2 process. D shows 1D plots of the spectra at 80, 160, 260, 320, and 420 K. E shows a color contour map of all 10-temperature data. The TRPL data at each temperature was fitted to a function of two-exponential terms convoluted with the instrumental resolution function. The results of the fit are shown as the lines in A and D, and the resulting lifetimes relevant to the band edge are plotted in C for HEAT1 and F for HEAT2 as a function of temperature. See *SI Appendix* for the details of the analysis.

orientation with large entropy in the cubic phase, as determined by the refinement of neutron data. Therefore, we conclude that the rotational motion of the organic molecule is central in the enhancement of the lifetime of the band-edge charge carriers.

For $CH_3NH_3PbI_3$, as shown in Fig. 6, the lifetime of the band-edge charge careers is $\tau(80\ K) = 60\ (3)$ ns at 80 K in the orthorhombic phase, which is comparable to the lifetime of the Tet LT phase of $HC(NH_2)_2PbI_3$, with both structures having direct bandgaps. Note that this is much shorter than the lifetime of the low-temperature hexagonal phase of $HC(NH_2)_2PbI_3$, $\tau_{hexLT}^{FAPbI_3}(80\ K) = 790\ (20)$ ns, with an indirect bandgap. Upon heating to 160 K, the TRPL intensity more rapidly decreases with increasing time (Fig. 6 A and B), indicating that the lifetime decreases to $\tau(160\ K) = 5.9\ (2)$ ns at 160 K (Fig. 6C) due to phonon scattering. Upon further heating, however, as the system enters its tetragonal phase $[T > 164\ (2)\ K]$, the TRPL lifetime abruptly jumps by a factor of 4 (see the 200 K data in Fig. 6A and the contour map of Fig. 6B), to $\tau(180\ K) = 24\ (2)$ ns (Fig. 6C). We note that this jump coincides with the activation of C_4 rotational mode of the MA^+ molecule in the tetragonal phase (21). Upon further heating up to 300 K, the TRPL intensity decreases more rapidly with increasing temperature (Fig. 6B) as seen in the 300 K data (Fig. 6A), as expected due to phonon scattering. The lifetime at 300 K is $\tau(300\ K) = 6.4\ (3)$ ns. On the other hand, as $CH_3NH_3PbI_3$ enters its cubic phase for $T > 320$ K, the lifetime increases (see the 360 K data in Fig. 6A and the contour map of Fig. 6B) to $\tau(T > 320\ K) \sim 11\ (3)$ ns (Fig. 6C). This small increase is also correlated with the small increase in rotational entropy of MA^+ molecules due to the presence of preferential orientations even in the cubic phase (21).

Discussion

The observation that the band-edge lifetime increases in the cubic phases of both $HC(NH_2)_2PbI_3$ and $CH_3NH_3PbI_3$ indicates the universality of the role of rotational motion of organic molecule in the HOIPs. The increase by a factor of ~2 at ~320 K as $CH_3NH_3PbI_3$ transits from tetragonal to cubic phase is similar to but much smaller than the jump by a factor of ~10 observed for the tetragonal-to-cubic phase transition of $HC(NH_2)_2PbI_3$. The different increases in lifetime in the two systems are due to the different geometries of the linear $CH_3NH_3^+$ and the ~120° bent $HC(NH_2)_2^+$. First, the liner $CH_3NH_3^+$ has an electric dipole

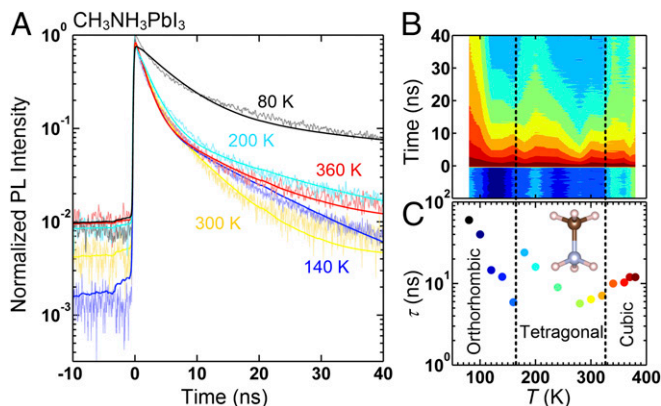**Fig. 6.** Time-resolved photoluminescence (TRPL) spectra of $CH_3NH_3PbI_3$. The TRPL spectra were taken at 15 different temperatures. A shows 1D plots of the spectra at 80, 140, 200, 300, and 360 K. B shows a color contour map of all 15 temperature datasets. The TRPL data at each temperature was fitted to a function of two-exponential terms convoluted with the instrumental resolution function. The results of the fit are shown as the lines in A, and the resulting lifetimes relevant to the band edge are plotted in C as a function of temperature.

moment $p = 2.3$ D (D denotes Debye) and a weaker quadrupole moment $Q_{ii} = (-1.8,\ -1.8,\ 3.6)$D·Å, whereas the bent $HC(NH_2)_2^+$ has a weak $p = 0.35$ D and a very strong quadrupole moment $Q_{ii} = (-18.3,\ 12.4,\ 5.8)$D·Å, where the coordinates were chosen to have zero off-diagonal Q_{ij} (32). See *SI Appendix*, Fig. S10, for the electric charge density distribution in the molecules. Previously, only the dipole moments of $CH_3NH_3^+$ and $HC(NH_2)_2^+$ were considered, and $CH_3NH_3^+$ was considered to be more relevant in charge screening mechanism. However, the strong quadrupole moment of $HC(NH_2)_2^+$ can produce the electric field at nearby lead and iodine sites that is comparable with the electric field of the dipole moment of $CH_3NH_3^+$. Second, in the cubic phase of $CH_3NH_3PbI_3$ the $CH_3NH_3^+$ molecule has preferential orientations (21), whereas in the cubic phase of $HC(NH_2)_2PbI_3$ the $HC(NH_2)_2^+$ has no preferential orientation (23). Thus, it is easier for $HC(NH_2)_2^+$ molecules to change their orientations in response to a presence of photoexcited charge carriers to maximize the screening effect due to the dipole and quadrupole moments, yielding the observed more enhanced increase in the charge carrier lifetime than in $CH_3NH_3^+$.

We note that there have been recent papers that suggest the role of screening by the inorganic atoms (33–35) or acoustic-optical phonon up-conversion involving both organic and inorganic atoms (36) in increasing the carrier lifetime in metal halide perovskites. These mechanisms may contribute to the long carrier lifetime. In searching for a signature of inorganic atoms and phonons increasing the PL lifetime, we have analyzed our neutron and X-ray diffraction data to show the temperature dependence of thermal factors, which is a measure of local atomic fluctuations. As shown in *SI Appendix*, Figs. S11 and S12, the thermal factors of inorganic atoms and organic molecules do not show any abrupt anomalies at the phase transition temperatures where we observe sudden jumps in PL lifetime. Even though further studies are necessary, we believe this suggests that the contributions from the local fluctuations of inorganic atoms and phonons are not responsible for the abrupt jump observed in PL lifetime. We emphasize that the carrier lifetime abruptly increases only when the systems transits from a phase with low rotational entropy of organic molecules to a phase with high rotational entropy, for instance, the orthorhombic–tetragonal transition for MAPbI₃ (Fig. 6C) and the tetragonal/hexagonal–cubic transition for FAPbI₃ (Fig. 5 C and F). It is possible that several factors contribute to the long lifetime of the charge carriers in HOIPs. Our experimental findings, however, clearly show that the organic cations play a major role.

Long lifetime of band-edge carriers is what makes HOIP solar cells highly efficient, despite their modest carrier mobility. Our observation of the increased lifetime in the cubic phase of $HC(NH_2)_2PbI_3$ and $CH_3NH_3PbI_3$ with higher rotational entropy of organic cations and larger thermal energy suggests that ferroelectric domain formation is not likely to be responsible. It is because, even if ferroelectric domains are formed in the lower symmetry phases at lower temperatures (8, 37), such domains are expected to disappear in the high-symmetry cubic phase (37). Among other mechanisms that have been proposed to explain the long lifetime, our results support the scenario of formation of large polarons, which is consistent with the long carrier lifetime but modest carrier mobilities observed in HOIPs (14–16). Such screening phenomena are not rare. The most well-known example is the electron–phonon coupling in the conventional type I superconductors (SCs). In the type I SC, the repulsion between electrons becomes effectively attractive due to the lattice vibrations. Here, in HOIPs, the attraction between electron and hole becomes effectively repulsive due to the screening by the organic molecules. The bound state in the SC is a Cooper pair. The bound state in HOIPs is most likely polarons.

1. Jeon NJ, et al. (2015) Compositional engineering of perovskite materials for high-performance solar cells. *Nature* 517:476–480.
2. Saliba M, et al. (2016) Cesium-containing triple cation perovskite solar cells: Improved stability, reproducibility and high efficiency. *Energy Environ Sci* 9:1989–1997.
3. Yang WS, et al. (2015) SOLAR CELLS. High-performance photovoltaic perovskite layers fabricated through intramolecular exchange. *Science* 348:1234–1237.
4. Zhou H, et al. (2014) Photovoltaics. Interface engineering of highly efficient perovskite solar cells. *Science* 345:542–546.
5. Brenner TM, Egger DA, Kronik L, Hodes G, Cahen D (2016) Hybrid organic–inorganic perovskites: Low-cost semiconductors with intriguing charge-transport properties. *Nat Rev Mater* 1:15007.
6. Frost JM, et al. (2014) Atomistic origins of high-performance in hybrid halide perovskite solar cells. *Nano Lett* 14:2584–2590.
7. Frost JM, Butler KT, Walsh A (2014) Molecular ferroelectric contributions to anomalous hysteresis in hybrid perovskite solar cells. *APL Mater* 2:081506.
8. Kutes Y, et al. (2014) Direct observation of ferroelectric domains in solution-processed $CH_3NH_3PbI_3$ perovskite thin films. *J Phys Chem Lett* 5:3335–3339.
9. Liu S, et al. (2015) Ferroelectric domain wall induced band gap reduction and charge separation in organometal halide perovskites. *J Phys Chem Lett* 6:693–699.
10. Etienne T, Mosconi E, De Angelis F (2016) Dynamical origin of the Rashba effect in organohalide lead perovskites: A key to suppressed carrier recombination in perovskite solar cells? *J Phys Chem Lett* 7:1638–1645.
11. Hutter EM, et al. (2017) Direct-indirect character of the bandgap in methylammonium lead iodide perovskite. *Nat Mater* 16:115–120.
12. Zheng F, Tan LZ, Liu S, Rappe AM (2015) Rashba spin-orbit coupling enhanced carrier lifetime in $CH_3NH_3PbI_3$. *Nano Lett* 15:7794–7800.
13. Pazos-Outón LM, et al. (2016) Photon recycling in lead iodide perovskite solar cells. *Science* 351:1430–1433.
14. Chen Y, et al. (2016) Extended carrier lifetimes and diffusion in hybrid perovskites revealed by Hall effect and photoconductivity measurements. *Nat Commun* 7:12253.
15. Zhu H, et al. (2016) Screening in crystalline liquids protects energetic carriers in hybrid perovskites. *Science* 353:1409–1413.
16. Zhu XY, Podzorov V (2015) Charge carriers in hybrid organic-inorganic lead halide perovskites might be protected as large polarons. *J Phys Chem Lett* 6:4758–4761.
17. Filip MR, Eperon GE, Snaith HJ, Giustino F (2014) Steric engineering of metal-halide perovskites with tunable optical band gaps. *Nat Commun* 5:5757.
18. Chen C-Y, et al. (2017) All-vacuum-deposited stoichiometrically balanced inorganic cesium lead halide perovskite solar cells with stabilized efficiency exceeding 11. *Adv Mater* 29:1605290.
19. Nam JK, et al. (2017) Potassium incorporation for enhanced performance and stability of fully inorganic cesium lead halide perovskite solar cells. *Nano Lett* 17:2028–2033.
20. Sutton RJ, et al. (2016) Bandgap-tunable cesium lead halide perovskites with high thermal stability for efficient solar cells. *Adv Energy Mater* 6:1502458.
21. Chen T, et al. (2015) Rotational dynamics of organic cations in the $CH_3NH_3PbI_3$ perovskite. *Phys Chem Chem Phys* 17:31278–31286.
22. Weller MT, Weber OJ, Henry PF, Di Pumpo AM, Hansen TC (2015) Complete structure and cation orientation in the perovskite photovoltaic methylammonium lead iodide between 100 and 352 K. *Chem Commun* 51:4180–4183.
23. Chen T, et al. (2016) Entropy-driven structural transition and kinetic trapping in formamidinium lead iodide perovskite. *Sci Adv* 2:e1601650.
24. Foley BJ, et al. (2015) Temperature dependent energy levels of methylammonium lead iodide perovskite. *Appl Phys Lett* 106:243904.
25. Weller MT, Weber OJ, Frost JM, Walsh A (2015) Cubic perovskite structure of black formamidinium lead iodide, α-[HC(NH$_2$)$_2$]PbI$_3$, at 298 K. *J Phys Chem Lett* 6:3209–3212.
26. Kresse G, Furthmüller J (1996) Efficiency of ab-initio total energy calculations for metals and semiconductors using a plane-wave basis set. *Comput Mater Sci* 6:15–50.
27. Kresse G, Joubert D (1999) From ultrasoft pseudopotentials to the projector augmented-wave method. *Phys Rev B* 59:1758–1775.
28. Monkhorst HJ, Pack JD (1976) Special points for Brillouin-zone integrations. *Phys Rev B* 13:5188–5192.
29. Perdew JP, Burke K, Ernzerhof M (1996) Generalized gradient approximation made simple. *Phys Rev Lett* 77:3865–3868.
30. Umari P, Mosconi E, De Angelis F (2014) Relativistic GW calculations on $CH_3NH_3PbI_3$ and $CH_3NH_3SnI_3$ perovskites for solar cell applications. *Sci Rep* 4:4467.
31. Wright AD, et al. (2016) Electron-phonon coupling in hybrid lead halide perovskites. *Nat Commun* 7:11755.
32. Jackson JD (1998) *Classical Electrodynamics* (Wiley, New York), 3rd Ed.
33. Kulbak M, Cahen D, Hodes G (2015) How important is the organic part of lead halide perovskite photovoltaic cells? Efficient CsPbBr$_3$ cells. *J Phys Chem Lett* 6:2452–2456.
34. Yaffe O, et al. (2017) Local polar fluctuations in lead halide perovskite crystals. *Phys Rev Lett* 118:136001.
35. Zhu H, et al. (2017) Organic cations might not be essential to the remarkable properties of band edge carriers in lead halide perovskites. *Adv Mater* 29:1603072.
36. Yang J, et al. (2017) Acoustic-optical phonon up-conversion and hot-phonon bottleneck in lead-halide perovskites. *Nat Commun* 8:14120.
37. Rakita Y, et al. (2017) Tetragonal $CH_3NH_3PbI_3$ is ferroelectric. arXiv:1702.05267.

Supporting Information

for

Origin of Long Lifetime of Band-Edge Charge Carriers in Organic-Inorganic Lead Iodide Perovskites

Tianran Chen, Wei-Liang Chen, Benjamin J. Foley, Jooseop Lee, Jacob Ruff, J. Y. Peter Ko, Craig M. Brown, Leland W. Harriger, Depei Zhang, Changwon Park, Mina Yoon, Yu-Ming Chang, Joshua J. Choi, and Seung-Hun Lee

This PDF file includes:

Sample Preparation

Experimental procedure of the photoluminescence measurements

Experimental procedure and analysis of the time-resolved photoluminescence

Neutron scattering methods and data

Synchrotron x-ray scattering method and data

Density functional theory Calculations

Temperature dependence of thermal factors

Sample preparation

PbI_2 (99.999%) in a powder form and gamma-butyrolactone (gBL) (99%) in a liquid form were purchased from Sigma-Aldrich. Formamidinium iodide ($HC(NH_2)_2I$) and methylammonium iodide (MAI) in a powder form were purchased from Dyesol.

3.58 grams of $HC(NH_2)_2PbI_3$ and 9.38 grams of PbI_2 were added to 30 mL of gBL. The solution was dissolved at 150 °C, and heated at the same temperature in ambient conditions for approximately 8 hours in an evaporating dish until the solvent had evaporated and black crystals were visible. The sample was then cooled to room temperature, and the yellow solid was collected and further dried in a nitrogen glovebox for 2 hours at 100 °C. 12.47 grams of yellow powder were collected. This powder turned back upon heating to 170 °C, and returned to its original color upon cooling. $CH_3NH_3PbI_3$ was synthesized using the same method as reported before (S1).

Experimental procedure of the photoluminescence measurements

The temperature dependent photoluminescence (PL) measurements were performed on a custom-built laser scanning confocal system coupled to a temperature controlled vacuum stage (Linkam THMS350V). The excitation from a 450 nm pico-second pulsed laser with a repetition rate of 1 MHz, was focus with a 5× objective (Olympus, MPLanFL N, NA 0.15) onto the sample. The on-sample power was ~0.4 μW. The PL spectra were acquired using a custom-built spectrometer with a thermoelectric-cooled CCD (Andor iDus). Spectra were obtained 2 minutes after reaching each set temperature. For better statistics, we used the average spectrum from a 5×5 spectral mapping covering an area of 56×56 μm^2. The integration time for each spectrum was 4 s.

Fig. S1 shows the Full-Width-at-Half-Maximum (FWHM) of the main emission peaks of the PL data (see Fig. 1) taken from a powder sample of $HC(NH_2)_2PbI_3$ for HEAT1 (blue circles) and HEAT2 (red squares). For HEAT2, there exist two emission peaks around 1.46 eV for $140\,K \leq T \leq 220\,K$. The FWHMs of the two peaks are similar and in Fig. S1 only the FWHM of the stronger peak is shown.

Fig. S2 shows the Full-Width-at-Half-Maximum (FWHM) of the main emission peaks of the PL data (see Fig. 2) taken from a powder sample of $NH_3CH_3PbI_3$. The FHWMs are similarly narrow

as those of the tetragonal and cubic phases of $HC(NH_2)_2PbI_3$. These indicate that the tetragonal and cubic phases of both HOIPs have direct bandgap.

Experimental procedure and analysis of the time-resolved photoluminescence

For the time-resolved photoluminescence (TRPL) measurements, the PL signal from the sample was sent into a custom-built monochromator coupled with a photomultiplier tube (PMT) detector, allowing for TRPL measurement of the desired wavelength of the PL spectrum. The monochromator contains an adjustable detection slit that was set for a 15 nm bandwidth detection. Finally, the PMT signal was sent to the time correlated single photon counting (TCSPC) device (PicoQuant, PicoHarp 300) for TRPL measurements.

To determine the PL lifetime, we used the commercial software FluoFit (PicoQuant), and fitted the TRPL data to a two-exponential re-convolution function

$$I(t) = \int_{-\infty}^{t} IRF(t') \left[A_1 e^{-\frac{t-t'}{\tau_1}} + A_2 e^{-\frac{t-t'}{\tau_2}} \right] dt' \qquad (1)$$

Here t is the delay time between the laser pulse and PL emission, IRF is the instrument response function, and A_1, A_2 and τ_1, τ_2 are the amplitude and lifetime of the exponential components respectively. The thick smooth lines in Fig. 5 and 6 are the fitting results and the fitted parameters are listed in Tables S1, S2, and S3. In our system, the IRF has a FWHM of 0.3 ns. When the lifetime approaches that of the IRF, the TRPL curve would show features of the IRF. The phenomenological fitting employed here does not distinguish the first, second and third order kinetics that have been assigned to trap-mediated recombination, radiative biomolecular recombination and Auger recombination respectively (S2). Distinguishing them requires a detailed TRPL study with various excitation light fluence at each temperature, which is beyond the scope of this work. Instead, our approach here was to study the temperature dependence of TRPL with the same sample in which the defect density is expected to increase monotonically with temperature. Thus, the observed discontinuous anomalous lifetime behaviors as a function of temperature cannot be explained in terms of defect density. In particular, the jump in lifetime by up to two orders of magnitude when the system enters the high organic cation rotation entropy phase warrants that our analysis is sufficient for the purpose of this work. Nonetheless, further

studies on detailed TRPL measurements and analysis as a function of excitation light intensity and temperature will be valuable.

Neutron scattering methods and data

NIST NCNR SPINS: The elastic neutron scattering data were obtained at the cold neutron triple-axis spectrometer, SPINS at the NIST Center for Neutron Research (NCNR) located in Gaithersburg, Maryland. Each of non-deuterated $HC(NH_2)_2PbI_3$ (~10 g) and $CH_3NH_3PbI_3$ (~10 g) sample was placed into a cylindrical aluminum can in a dry helium box. The aluminum can was sealed with a lead o-ring. The sample can was mounted in a closed cycle helium 2rigerator and the temperature was changed in the range of 8.2 K – 450 K. The energy of the neutrons was 5 meV. The collimations were open - 80'- 80'- open, from the cold neutron guide to the monochromator to the sample to the analyzer to the detector. The higher order neutron contaminations were eliminated by placing two liquid nitrogen cooled beryllium filters before and after the sample.

Note that similar data obtained from deuterated $HC(ND_2)_2PbI_3$ have been reported in Ref. (S3). The hexagonal-to-cubic phase transition temperature for non-deuterated $HC(NH_2)_2PbI_3$, $T_{cubic}^{HEAT1} = 400(20)$ K (see Fig. 3A and 3B), is higher than that for $HC(ND_2)_2PbI_3$ that is 350(5) K. The difference in T_{cubic}^{HEAT1} is due to the fact that the transition is driven by the entropy caused by the isotropic rotations of the FA^+ cation, $S_{rot} = \frac{3}{2} k_B \{1 + \ln(0.4786 \, k_B T \sqrt[3]{I_1 I_2 I_3})\}$ where k_B is the Boltzmann constant; $HC(NH_2)_2PbI_3$ has smaller principle moment of inertia $\left(I_i \approx 8.586, 48.851, 57.436 \text{ u\AA}^2\right)$ than $HC(ND_2)_2PbI_3$ does $\left(I_i \approx 11.644, 60.161, 71.806 \text{ u\AA}^2\right)$ where the unified atomic mass unit, u, is $1.6605e^{-27}$ kg. Thus, their temperature difference in the entropy-driven transition is estimated to be $\Delta T_c = 55$ K, which is consistent with our experimental observation.

Fig. S3 shows the elastic neutron scattering data obtained from $NH_3CH_3PbI_3$ as a function of temperature. $NH_3CH_3PbI_3$ undergoes an orthorhombic-to-tetragonal phase transition at 164(2) K, and a tetragonal-to-cubic phase transition at 325(3) K.

NIST NCNR BT1: To determine the crystal structures of the quenched phases, neutron powder diffraction (NPD) measurements were performed, using the BT1 diffractometer at NCNR. The

wavelength of incident neutrons, $\lambda = 1.5398$ Å, was selected using a Cu (311) monochromator with an in-pile 60' collimator. The scattered neutrons were collected by 32 3-He detectors over the 2θ range of 1.3°– 166.3° with 0.05° step size. A 10 g sample of $HC(ND_2)_2PbI_3$ was placed into a cylindrical vanadium can in a dry helium box. The vanadium can was sealed with an indium o-ring. The sample can was mounted in a closed cycle helium refrigerator.

Fig. S4 shows the neutron diffraction pattern obtained at 100 K (Tet LT) and 200 K (Tet IT) in the HEAT1 process. The main difference between 100 K and 200 K is that at 100 K there exists a set of superlattice peaks that can be indexed with a characteristic wave vector of $q = \left(0,0,\frac{1}{6}\right)$. The data were refined simultaneously with synchrotron x-ray data shown in Fig. S4 to determine the quenched structures to be tetragonal; the $P4/mbm$ tetragonal (Tet LT) for $T < T_{Tet\ LT}^{HEAT2} = 140(10)$ K and the $P4bm$ tetragonal (Tet IT) for $T_{Tet\ LT}^{HEAT2} < T < T_{Cubic}^{HEAT2}$. The crystal structures of the Tet IT and Tet LT phases were determined by simultaneous refinement of the neutron diffraction data and the x-ray data shown as solid lines in Fig. S4 and S5. Their structural parameters are listed in Table S3 (Tet IT) and S4 (Tet LT). Here we emphasize that the neutron powder diffraction refinement result shows that $HC(NH_2)_2^+$ cations in Tet IT phase have strongly preferential orientations (see Fig. 4C). On the contrary, $HC(NH_2)_2^+$ cations have isotropic orientations in the cubic phase (see Fig. 4A) (S3).

Synchrotron x-ray scattering methods and data

Synchrotron x-ray powder diffraction has been measured at the F2 beam line at the Cornell High Energy Synchrotron Source (CHESS). Diffraction patterns with the Q range from 0.3 Å^{-1} to 9.3 Å^{-1} were collected with incident wavelength 0.202153 Å and a 2D flat panel detector. The powder was sealed inside a 1 mm diameter Kapton capillary, and was rotated 360° during data collection to achieve ideal powder averaging.

The sample of $HC(NH_2)_2PbI_3$ was heated *ex situ* for 30 minutes at 450K, where the color fully turned black. It then was cooled down to 100 K at the rate of 4 K/min using a liquid nitrogen cryostream. The data were collected while warming the sample from 100 K to 300 K with 25 K steps. Each measurement involved 12 rotations amounting to 2.5 hours beam exposure for every temperature step.

Table S3 and S4 in the Supporting Information list the structural parameters for the Tet LT and Tet IT phases of $HC(NH_2)_2PbI_3$.

Fig. S5 shows the synchrotron X-ray powder diffraction data at three different temperatures, 300 K (cubic phase), 200 K (Tet IT phase) and 100 K (Tet LT phase). As shown in the lower panel, the Tet LT phase exhibit a set of weak supperlattice peaks characterized with $q = \left(0,0,\frac{1}{6}\right)$. This means that the Tet LT phase adopts a 1×1×6 supercell, compared to the Tet IT phase.

Fig. S6 summarizes the temperature dependence of the lattice constants of $FAPbI_3$: the lattice constants determined with neutron diffraction data (squares) and with synchrotron x-ray data (triangles).

Density Functional Theory Calculations

Our first principles density functional theory calculations (DFT) use projector augmented wave (S4) to describe the core electrons and the generalized gradient approximation with the Perdew-Burke-Ernzerhof functional (S5), as implemented in VASP (Vienna *Ab initio* Simulation Package) code (S6). 4×4×4 k-points are sampled through Monkhorst-Pack scheme (S7) for cubic unit cell and equivalent and denser sampling was used for tetragonal and hexagonal unit cells.

The lattice constants and atomic coordinates are obtained from Rietveld refinement of X-ray and neutron diffraction experiments. Lead (Pb) and Iodine (I) atoms are fixed and $HC(NH_2)_2^+$ cations are fully relaxed until the force on each atom is less than 0.02 eV/Å. However, since the optimization is performed at zero temperature, $HC(NH_2)_2^+$ cations remain frozen at the local minimum near the assigned orientation. Such a frozen $HC(NH_2)_2^+$ cation can locally break the cubic/tetragonal/hexagonal symmetry, thus the calculated formation entropy and electronic band structures have some ambiguity in our calculation settings. After the fully relaxation of $HC(NH_2)_2^+$ cations is reached, non-self-consistent field calculation is performed and electronic band structures are calculated on selected k-point-paths (Γ-X-M-Γ-R-X for cubic structure, Γ-K-H-A-Γ-M-L-A for hexagonal structure, and Γ-X-M- Γ-Z-R-A for tetragonal structure).

Fig. S7 shows the electronic band structure of $HC(NH_2)_2PbI_3$ for the cubic, Hex IT and Tet IT phases. We note that for the cubic phase we assumed a ferro-oriented pattern of the FA^+ actions in which the planar FA^+ cations lie in the central mirror plane of the unit cell and the C–H bond

is directed into a cube face. The orientations of each FA^+ cation in different unit cells were assumed to be the same. This was necessary for the limitation of DFT calculations being done at zero temperature. For other phases the DFT calculations were performed on the experimentally determined structures. Fig. S8 shows the electronic band structures for the Hex LT and Tet LT phases that were obtained by DFT calculations. The crystal structures for Hex IT phases were taken from Ref. (S3), while the crystal structure of the Tet LT phase was determined by Rietveld refinement of neutron diffraction and synchrotron x-ray data taken at 100 K. Tet LT phase has sharp cone-shape bands with direct bandgap, similar to Tet IT phase. In contrast, the Hex LT phase has nearly flat valence and conduction bands with indirect bandgap, similar to Hex IT phase. This is consistent with the PL data shown in the main text.

Fig. S9 shows the calculated electronic band structures for the cubic, tetragonal, and orthorhombic phases of $CH_3NH_3PbI_3$. All phases show similar direct band gaps, which is consistent with their PL data shown in Fig. 2 and S2.

The electronic charge densities of $CH_3NH_3^+$ and $HC(NH_2)_2^+$ cations were calculated using VASP package. Pb and I atoms were not involved in the calculation. Instead, a constant charge density background was added to neutralize the cation. In order to show clearly the electric polarity in the molecule, the calculated charge density was then subtracted from a direct sum of single-atom charge densities of each atom (which have negligible dipole and quadrupole moment). The subtracted "excessive" charge density is plotted in Fig. S10. The blue and red surfaces are isosurfaces of "excessive" electrons and holes, respectively.

Analysis of thermal factors

Isotropic thermal factors of Pb, I and organic cation of $FAPbI_3$ (Fig. S11) and $MAPbI_3$ (Fig. S12) as a function of temperature were obtained through Rietveld refinement of synchrotron X-ray and neutron diffraction data. As shown in Fig. S11 and S12, the thermal factors of inorganic atoms and organic molecules do not show any abrupt anomalies at the phase transition temperatures where we observe sudden jumps in PL lifetime. This suggests that the contributions from the local fluctuations of inorganic atoms and phonons are not responsible for the abrupt jump observed in PL lifetime.

References

S1.   Zhu H, *et al*. (2016) Screening in crystalline liquids protects energetic carriers in hybrid perovskites. *Science* 353(6306):1409-1413.

S2.   Stranks SD, *et al*. (2014) Recombination Kinetics in Organic-Inorganic Perovskites: Excitons, Free Charge, and Subgap States. *Phys. Rev. Applied* 2(3):034007.

S3.   Chen T, *et al*. (2016) Entropy-driven structural transition and kinetic trapping in formamidinium lead iodide perovskite. *Science Advances* 2(10):e1601650.

S4.   Kresse G & Joubert D (1999) From ultrasoft pseudopotentials to the projector augmented-wave method. *Phys. Rev. B* 59(3):1758-1775.

S5.   Perdew JP, Burke K, & Ernzerhof M (1996) Generalized Gradient Approximation Made Simple. *Phys. Rev. Lett.* 77(18):3865-3868.

S6.   Kresse G & Furthmüller J (1996) Efficiency of ab-initio total energy calculations for metals and semiconductors using a plane-wave basis set. *Computational Materials Science* 6(1):15-50.

S7.   Monkhorst HJ & Pack JD (1976) Special points for Brillouin-zone integrations. *Phys. Rev. B* 13(12):5188-5192.

S8.   Chen T, *et al*. (2015) Rotational dynamics of organic cations in the $CH_3NH_3PbI_3$ perovskite. *Phys. Chem. Chem. Phys.* 17(46):31278-31286.

S9.   Weller MT, Weber OJ, Henry PF, Pumpo AMD, & Hansen TC (2015) Complete structure and cation orientation in the perovskite photovoltaic methylammonium lead iodide between 100 and 352 K. *Chem. Commun.* 51(20):4180-4183.

Tables

Table S1. HC(NH$_2$)$_2$PbI$_3$: Fitted parameters for TRPL of HEAT1. Results of reconvolution fit for the TRPL of HEAT1 measurements. For 420K and 440K, the TRPL integration time was 3 minutes. For all other temperatures, the integration time was 1 minute.

Temperature (K)	Detection Wavelength (nm)	A$_1$	τ$_1$ (ns)	A$_2$	τ$_2$ (ns)	Background
80	680	120(4)	790(20)	110(100)	4(4)	16(1)
120	660	110(10)	110(10)	90(30)	30(10)	7.3(5)
140	660	250(40)	22(2)	880(120)	6.2(8)	7.7(5)
160	700	90(30)	11(4)	350(150)	1.6(7)	7.9(5)
200	680	25(26)	11(12)	600(200)	1.1(4)	9.0(5)
240	670	60(40)	8(4)	3000(700)	0.45(9)	10.6(6)
280	660	150(110)	1.7(1)	4300(1500)	0.15(5)	8.1(5)
320	650	120(140)	1.1(10)	5600(2400)	0.08(3)	7.8(5)
360	640	73(130)	1(1)	7000(4300)	0.04(2)	7.5(5)
420	780	12(9)	120(120)	10(30)	15(40)	24.4(8)
440	790	16(5)	300(100)	30(40)	8(13)	22.7(8)

Table S2. HC(NH$_2$)$_2$PbI$_3$: Fitted parameters for TRPL of HEAT2. Results of reconvolution fit for the TRPL of HEAT2 measurements. For 420K, the TRPL integration time was 3 minutes. For all other temperatures, the integration time was 1 minute.

Temperature (K)	Detection Wavelength (nm)	A$_1$	τ$_1$ (ns)	A$_2$	τ$_2$ (ns)	Background
80	850	120(20)	39(6)	550(110)	4.4(9)	7.2(5)
120	830	150(25)	29(4)	1400(200)	3.4(4)	7.2(5)
160	840	22(15)	22(17)	120(70)	2.3(6)	6.7(5)
240	820	56(26)	11(5)	270(140)	1.4(7)	6.6(4)
260	820	96(19)	32(6)	590(130)	3.1(7)	6.9(5)
280	830	119(6)	310(15)	200(60)	9(3)	13.0(8)
320	820	34(5)	210(40)	170(50)	7(2)	8.9(6)
360	830	19(4)	230(60)	80(40)	6(4)	8.0(5)
400	800	20(4)	290(77)	70(40)	6(4)	7.6(5)
420	800	17(6)	260(110)	50(50)	6(7)	23.8(8)

Table S3. CH₃NH₃PbI₃: Fitted parameters for TRPL. Results of reconvolution fit for the TRPL data of $CH_3NH_3PbI_3$. The TRPL integration time was 3 minutes.

Temperature (K)	Detection Wavelength (nm)	A_1	τ_1 (ns)	A_2	τ_2 (ns)	Background
80	785	260(20)	60(3)	1600(100)	5.7(4)	8.6(8)
100	775	360(20)	40(2)	2600(200)	4.1(3)	8.3(7)
120	775	1200(80)	14.6(6)	12200(600)	1.88(9)	7.2(7)
140	775	1380(70)	12.1(4)	9700(500)	1.68(8)	7.6(9)
160	790	1560(80)	5.9(2)	3100(300)	1.4(1)	6.7(6)
180	785	160(20)	24(2)	2800(200)	1.8(1)	6.4(7)
200	780	180(20)	16(1)	1500(100)	2.3(2)	6.5(6)
240	770	1150(60)	9.0(3)	5300(300)	1.51(9)	6.6(6)
280	770	320(40)	5.7(5)	3600(300)	0.72(6)	6.0(5)
300	770	770(50)	6.4(3)	2800(200)	1.5(1)	5.9(5)
320	770	570(50)	7.1(4)	3200(200)	1.5(1)	5.8(5)
340	770	90(20)	10(2)	730(90)	1.5(1)	5.5(4)
360	770	190(20)	10.3(9)	1400(100)	1.5(1)	5.7(5)
370	760	40(10)	12(3)	640(80)	1.5(1)	5.5(4)
380	770	30(10)	12(4)	270(60)	1.5(1)	5.5(4)

Table S4. HC(NH₂)₂PbI₃: Refined structural parameters of HC(NH₂)₂PbI₃ Tet IT phase for 200 K. Positions within tetragonal $P4/mbm$ and occupancies per chemical unit cell (c.u.) in FAPbI₃ at $T = 200$ K were determined using Rietveld analysis of neutron diffraction data shown in Fig. 1 and 2. The lattice parameters are $a = 8.9258(3)$ Å, $c = 6.3259(4)$ Å. $\chi^2 = 0.8673$.

Atom	Wyck	x	y	z	Occ	$U_{iso}(\text{Å}^2)$
Pb	2a	0	0	0	1	0.019(1)
I1	2b	0	0	0.5	1	0.040(1)
I2	4g	0.7165(5)	0.7835(5)	0	1	=I1 U_{iso}
N1	16l	0.4368(88)	0.8967 (68)	0.4524(104)	1/8	0.088(3)
N2	16l	0.5752(83)	0.1161(72)	0.4612(120)	1/8	=N1 U_{iso}
C	16l	0.5293(32)	0.9900(41)	0.5429(29)	1/8	=N1 U_{iso}
H	16l	0.5715(168)	0.9600(150)	0.6998(162)	1/8	=N1 U_{iso}
D1	16l	0.3897(66)	0.9123(64)	0.3059(68)	1/8	=N1 U_{iso}
D2	16l	0.6476(58)	0.1802(78)	0.5463(79)	1/8	=N1 U_{iso}
D3	16l	0.4087(50)	0.8014(58)	0.5312(123)	1/8	=N1 U_{iso}
D4	16l	0.5437(46)	0.1564(52)	0.3156(89)	1/8	=N1 U_{iso}

Table S5. HC(NH$_2$)$_2$PbI$_3$: Refined structural parameters of HC(NH$_2$)$_2$PbI$_3$ Tet LT phase for 100 K. Positions within hexagonal $P4bm$ and occupancies per chemical unit cell (c.u.) in FAPbI$_3$ at $T = 100$ K were determined using Rietveld analysis of the neutron diffraction data shown in Fig. 1C. The lattice parameters are $a = 8.8774(1)$ Å, $c = 37.6724(14)$ Å. $\chi^2 = 1.270$.

Atom	Wyck	x	y	Z	Occ	$U_{iso}(Å^2)$
Pb1	2a	0	0	0.0016(7)	1	0.007(1)
Pb2	2a	0	0	0.5034(6)	1	=Pb1 U_{iso}
Pb3	2a	0	0	0.8320(5)	1	=Pb1 U_{iso}
Pb4	2a	0	0	0.3384(5)	1	=Pb1 U_{iso}
Pb5	2a	0	0	0.1672(6)	1	=Pb1 U_{iso}
Pb6	2a	0	0	0.6698(6)	1	=Pb1 U_{iso}
I1	2a	0	0	0.4180(15)	1	0.030(1)
I2	2a	0	0	0.9170(15)	1	=I1 U_{iso}
I3	4c	0.7857(24)	0.2857(24)	0.1618(11)	1	=I1 U_{iso}
I4	4c	0.7927(22)	0.2927(22)	0.6683(13)	1	=I1 U_{iso}
I5	2a	0	0	-0.7475(15)	1	=I1 U_{iso}
I6	2a	0	0	0.7543(14)	1	=I1 U_{iso}
I7	2a	0	0	0.5860(17)	1	=I1 U_{iso}
I8	2a	0	0	0.0881(16)	1	=I1 U_{iso}
I9	4c	0.8032(25)	0.3032(25)	-0.0004(14)	1	=I1 U_{iso}
I10	4c	0.7473(33)	0.2473(33)	0.4893(7)	1	=I1 U_{iso}
I11	4c	0.7840(22)	0.2840(22)	0.8294(11)	1	=I1 U_{iso}
I12	4c	0.7824(26)	0.2824(26)	0.3245(10)	1	=I1 U_{iso}
N1	8d	0.6061(133)	0.0805(162)	0.0846(124)	1/4	0.023(1)
N2	8d	0.4218(161)	-0.1040(137)	0.0860(124)	1/4	=N1 U_{iso}
N3	8d	0.5423(26)	-0.0016(60)	0.5812(5)	1/4	=N1 U_{iso}
N4	8d	0.4696(27)	-0.0138(61)	0.6402(5)	1/4	=N1 U_{iso}
N5	8d	0.6104(35)	-0.0557(39)	0.4092(8)	1/4	=N1 U_{iso}
N6	8d	0.3574(34)	-0.0348(38)	0.4234(8)	1/4	=N1 U_{iso}
N7	8d	0.5953(57)	0.0872(53)	0.9209(8)	1/4	=N1 U_{iso}
N8	8d	0.4201(57)	-0.1048(54)	0.9263(8)	1/4	=N1 U_{iso}
N9	8d	0.5849(39)	0.0838(41)	0.2547(10)	1/4	=N1 U_{iso}
N10	8d	0.3655(37)	-0.0400(38)	0.2387(11)	1/4	=N1 U_{iso}
N11	8d	0.5799(51)	0.0986(51)	0.7631(7)	1/4	=N1 U_{iso}
N12	8d	0.4074(51)	-0.0937(50)	0.7545(8)	1/4	=N1 U_{iso}
C1	8d	0.4672(59)	0.0354(56)	0.0885(8)	1/4	=N1 U_{iso}
C2	8d	0.4427(18)	-0.0225(35)	0.6062(5)	1/4	=N1 U_{iso}
C3	8d	0.4985(35)	0.0038(29)	0.4268(6)	1/4	=N1 U_{iso}
C4	8d	0.4972(40)	-0.0071(38)	0.9078(4)	1/4	=N1 U_{iso}
C5	8d	0.4967(37)	0.0188(34)	0.2316(6)	1/4	=N1 U_{iso}
C6	8d	0.4999(42)	0.0096(43)	0.7430(4)	1/4	=N1 U_{iso}
H1	8d	0.3821(182)	0.1212(167)	0.0942(20)	1/4	=N1 U_{iso}

|						
H2	8d	0.3275(21)	-0.0495(42)	0.5980(8)	1/4	=N1 U_{iso}
H3	8d	0.5250(50)	0.0932(49)	0.4458(12)	1/4	=N1 U_{iso}
H4	8d	0.4780(53)	-0.0039(56)	0.8791(5)	1/4	=N1 U_{iso}
H5	8d	0.5358(55)	0.0132(64)	0.2041(7)	1/4	=N1 U_{iso}
H6	8d	0.5112(54)	0.0225(54)	0.7142(4)	1/4	=N1 U_{iso}
D1	8d	0.6957(87)	0.0110(277)	0.0792(138)	1/4	=N1 U_{iso}
D2	8d	0.3104(210)	-0.1262(295)	0.0896(214)	1/4	=N1 U_{iso}
D3	8d	0.6285(294)	0.1924(218)	0.0871(214)	1/4	=N1 U_{iso}
D4	8d	0.4907(285)	-0.1943(91)	0.0808(139)	1/4	=N1 U_{iso}
D5	8d	0.6536(23)	0.0242(61)	0.5855(8)	1/4	=N1 U_{iso}
D6	8d	0.3831(35)	-0.0323(90)	0.6573(6)	1/4	=N1 U_{iso}
D7	8d	0.5084(40)	-0.0113(95)	0.5555(5)	1/4	=N1 U_{iso}
D8	8d	0.5728(35)	0.0106(73)	0.6511(6)	1/4	=N1 U_{iso}
D9	8d	0.5999(48)	-0.1402(55)	0.3907(12)	1/4	=N1 U_{iso}
D10	8d	0.2794(40)	0.0195(59)	0.4385(12)	1/4	=N1 U_{iso}
D11	8d	0.7161(34)	-0.0166(54)	0.4140(12)	1/4	=N1 U_{iso}
D12	8d	0.3184(40)	-0.1169(46)	0.4065(11)	1/4	=N1 U_{iso}
D13	8d	0.6230(65)	0.0951(64)	0.9473(10)	1/4	=N1 U_{iso}
D14	8d	0.3465(82)	-0.1729(77)	0.9132(13)	1/4	=N1 U_{iso}
D15	8d	0.6489(84)	0.1586(79)	0.9040(13)	1/4	=N1 U_{iso}
D16	8d	0.4282(67)	-0.1186(66)	0.9533(9)	1/4	=N1 U_{iso}
D17	8d	0.5608(56)	0.0959(68)	0.2812(10)	1/4	=N1 U_{iso}
D18	8d	0.3062(49)	-0.0879(62)	0.2186(15)	1/4	=N1 U_{iso}
D19	8d	0.6850(41)	0.1258(51)	0.2461(16)	1/4	=N1 U_{iso}
D20	8d	0.3167(43)	-0.0418(49)	0.2635(13)	1/4	=N1 U_{iso}
D21	8d	0.5791(60)	0.0974(60)	0.7904(7)	1/4	=N1 U_{iso}
D22	8d	0.3507(68)	-0.1568(65)	0.7364(11)	1/4	=N1 U_{iso}
D23	8d	0.6485(67)	0.1752(63)	0.7512(12)	1/4	=N1 U_{iso}
D24	8d	0.3872(59)	-0.1166(56)	0.7808(9)	1/4	=N1 U_{iso}
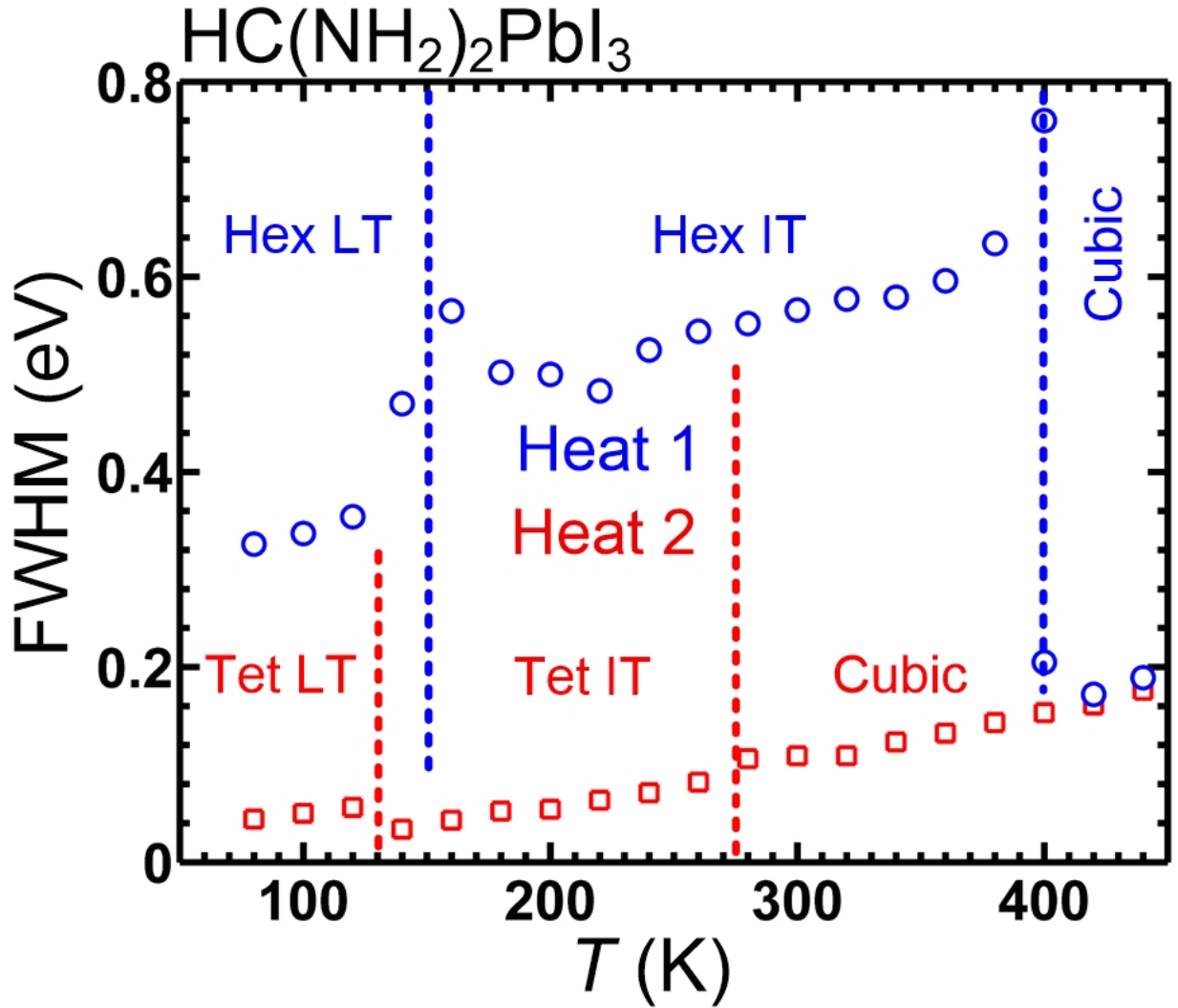
Fig. S1: Full-width-at-half-maximum (FWHM) of emission peaks of PL spectra of HC(NH$_2$)$_2$PbI$_3$. Blue circles and the red squares are the FWHMs of the main emission peaks of the PL data of HC(NH$_2$)$_2$PbI$_3$ shown in Fig. 1 for HEAT1 and HEAT2, respectively. For HEAT2, there exist two emission peaks for 140 K $\leq T \leq$ 220 K, and their FWHMs are similar and the FWHMs of the stronger peak are shown here.
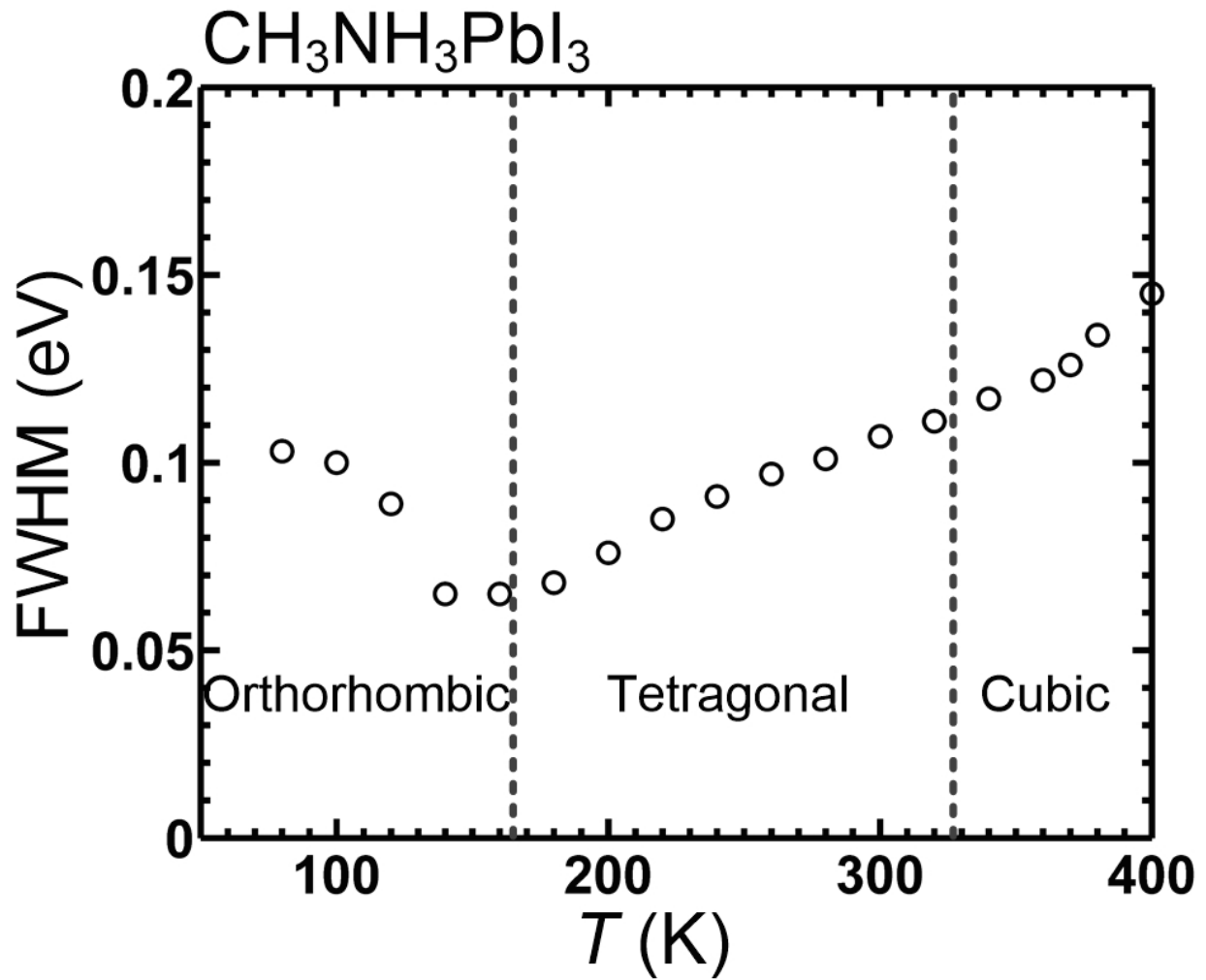
Fig. S2: Full-width-at-half-maximum (FWHM) of emission peaks of PL spectra of CH₃NH₃PbI₃. Blue circles and the red squares are the FWHMs of the main emission peaks of the PL data of CH₃NH₃PbI₃ shown in Fig. 2.
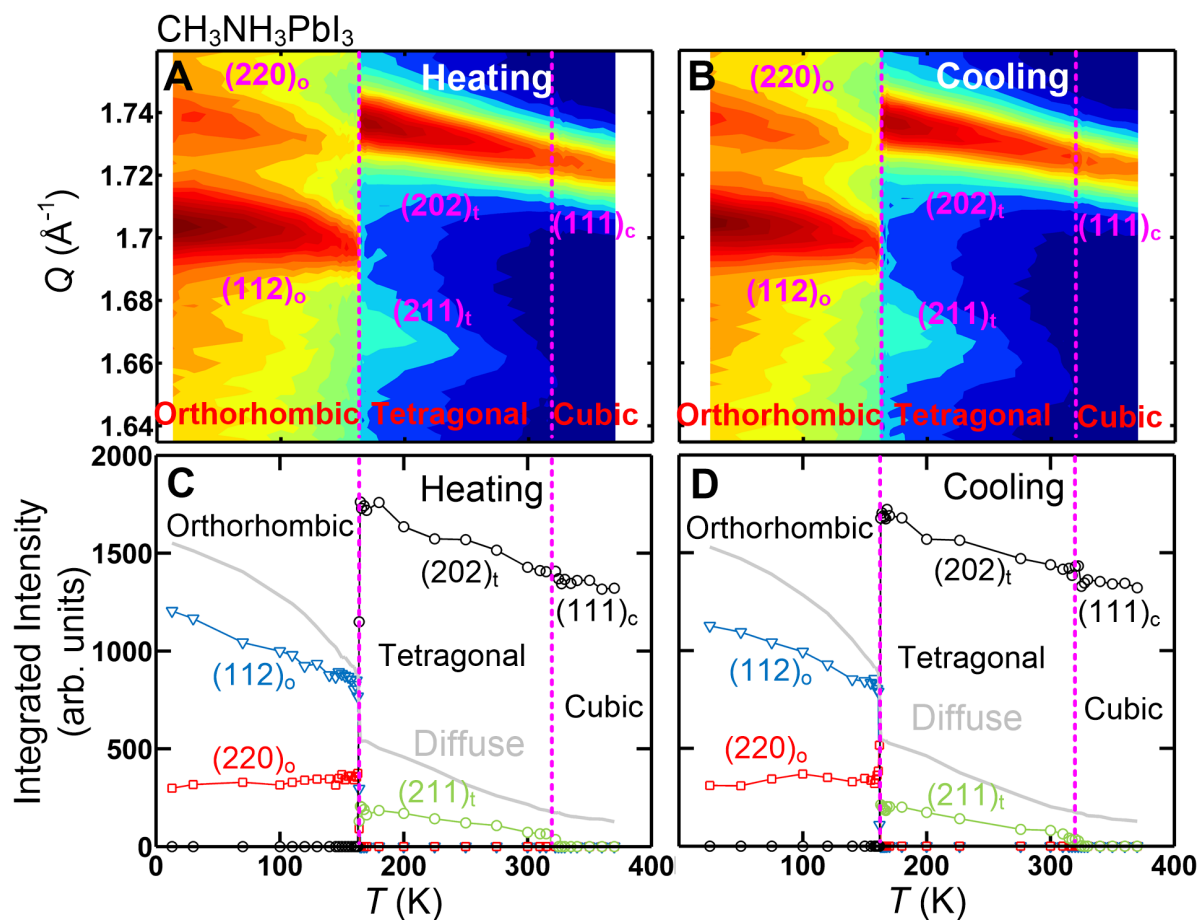
Fig. S3. Structural transitions of CH₃NH₃PbI₃. Elastic neutron scattering data were obtained at SPINS, NCNR. (*A*) and (*B*) shows a contour map of the scattering intensity as a function of momentum transfer, Q, and temperature, T. (*C*) and (*D*) shows the integrated intensities of the Bragg peaks as function of T.
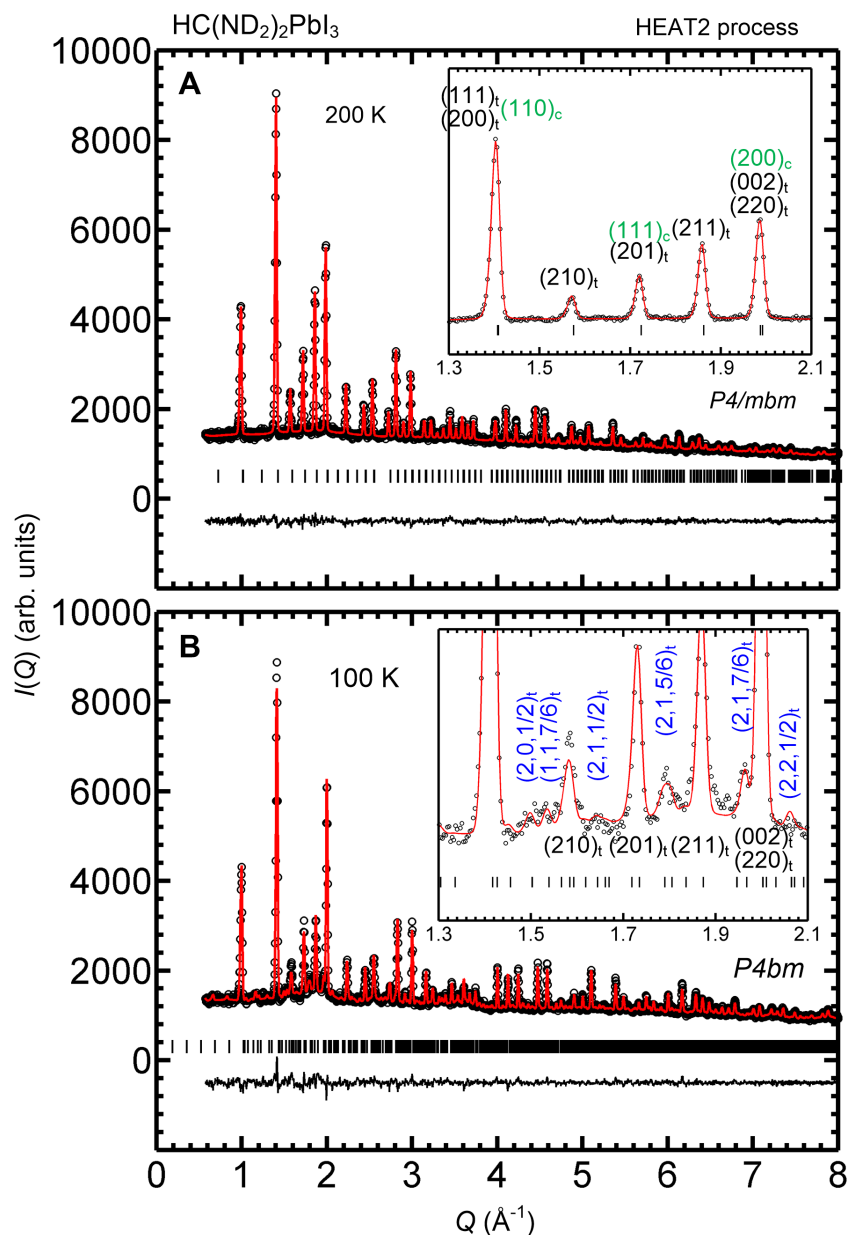
Fig. S4: HC(ND₂)₂PbI₃ neutron powder diffraction data. Data are obtained at BT1, NCNR. Neutron diffraction data taken at (*A*) 200 K (Tet IT phase) and (*B*) 100 K (Tet LT phase). The open circles, red lines, black tick marks, and black lines at the bottom are the experimental data, Rietveld refinement results, Bragg peak positions, and difference between the data and refinement, respectively. In the inset of (*A*), the Bragg peak positions expected for the high temperature cubic phase are written in green for comparison. In the inset of (*B*), the blue indices are the superlattice peaks allowed for the Tet LT phase with the characteristic wavevector of $q = (0,0,1/6)$ that are absent in Tet IT phase. The crystal structures of the Tet IT and Tet LT phases were determined by simultaneous refinement of the neutron diffraction data and the x-ray data. Their structural parameters are listed in Table S4 (Tet IT) and S5 (Tet LT).

Fig. S5
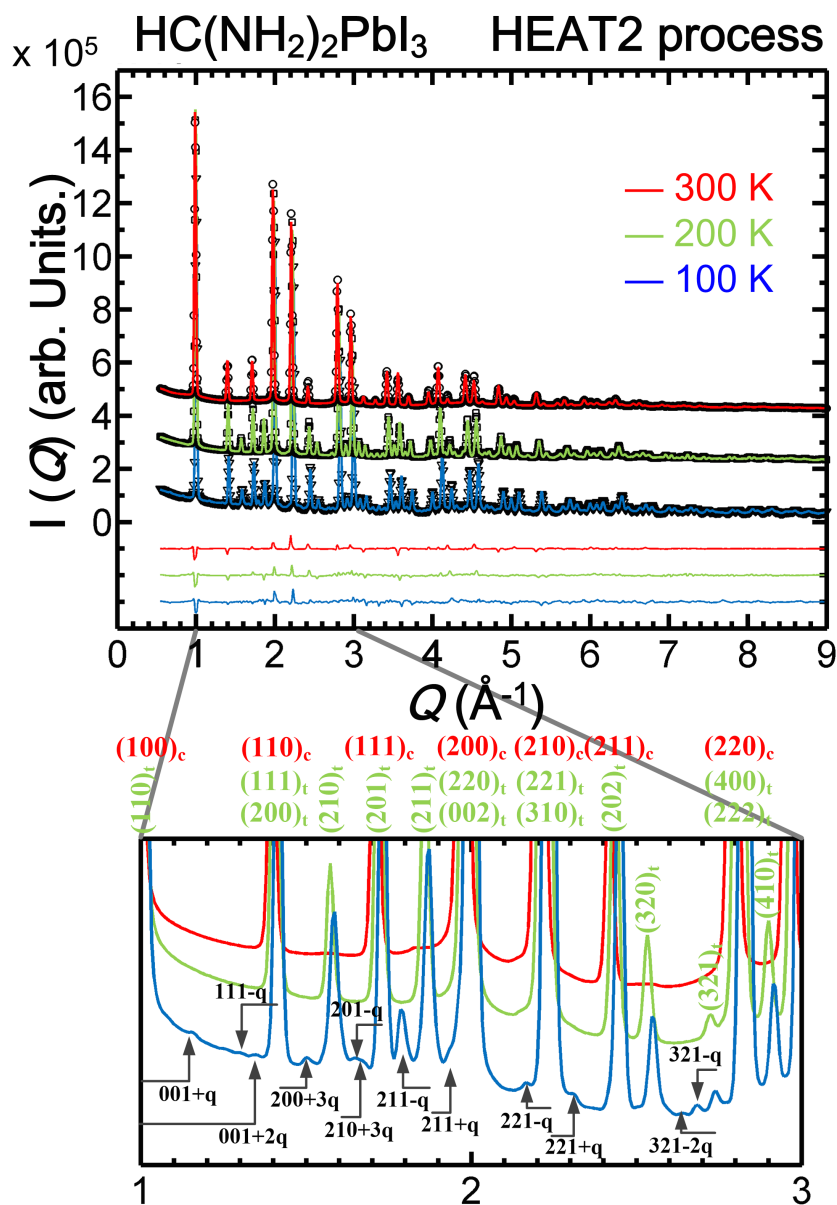
Fig. S5: HC(NH₂)₂PbI₃ synchrotron X-ray powder diffraction. Data are obtained at F2, CHESS. The upper panel shows the diffraction patterns obtained at 300 K (cubic phase), 200 K (Tet IT phase) and 100 K (Tet LT phase). The open symbols, thick colored lines over the symbols, and thin black lines at the bottom are the experimental data, Rietveld refinement results, and difference between the data and refinement, respectively. The lower panel shows an enlarged view of the data over a narrower range of Q from 1.0 Å^{-1} to 3.0 Å^{-1}. Red and green indices on the top are the Bragg peak positions of the cubic and Tet IT/Tet LT phases, respectively. The panel shows the weak supperlattice peaks with $q = (0,0,1/6)$ that are present in the Tet LT phase. This means that the Tet LT phase adopts a 1×1×6 supercell of the Tet IT phase.

Fig. S6
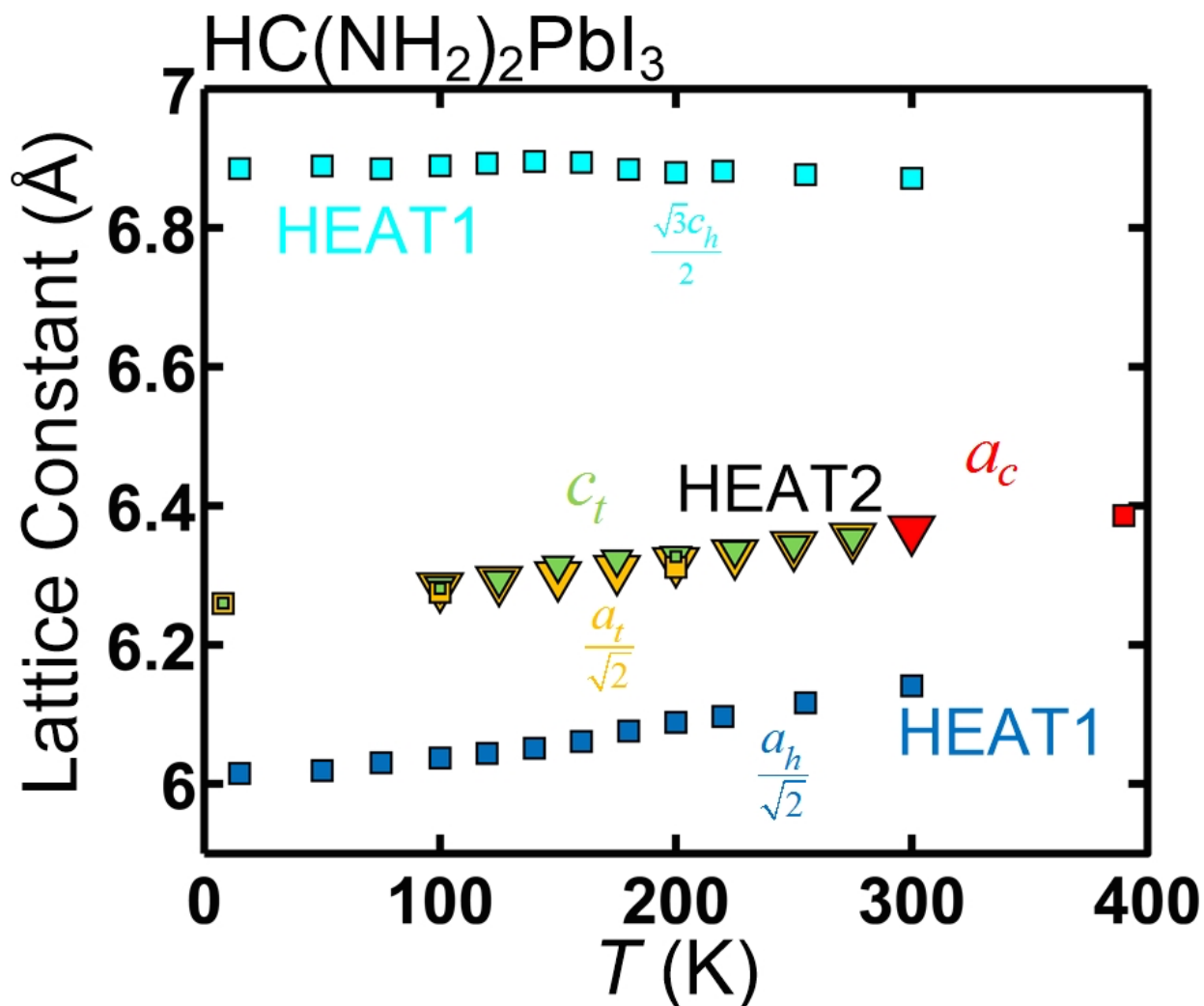
Fig. S6: Lattice constants of HC(ND₂)₂PbI₃ as a function of temperature. The lattice constants determined by the Rietveld refinements of neutron diffraction (squares) and synchrotron x-ray (triangles) data, some of which are shown in Fig. S4 and S5, are plotted as a function of temperature; red, orange, and green symbols are a_c, $\frac{a_t}{\sqrt{2}}$, c_t, respectively, where a_c is the cubic lattice constant, and a_t, c_t are the lattice constants of the Tet IT phase. The squares in cyan and blue are the lattice constants for the hexagonal phases, $\frac{a_h}{\sqrt{2}}$ and $\frac{\sqrt{2}c_h}{2}$, some of which have been reported in Ref. (S3).

Fig. S7
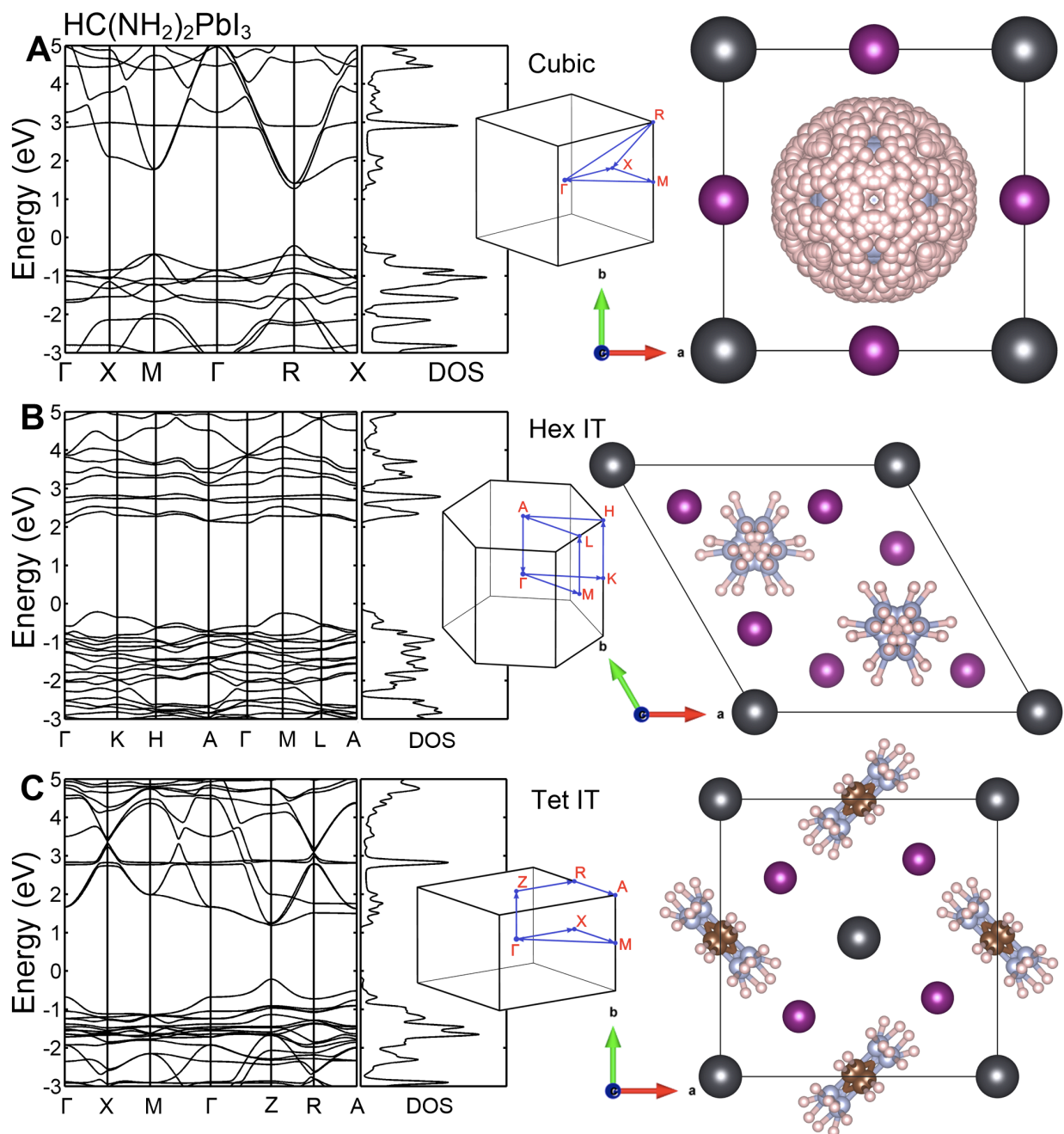
Fig. S7: Electronic band structure of HC(NH₂)₂PbI₃ for the cubic, Hex IT and Tet IT phases. Electronic band structures were obtained by DFT calculations for (*A*) the cubic, (*B*) Hex IT and (*C*) Tet IT phases of HC(NH₂)₂PbI₃.

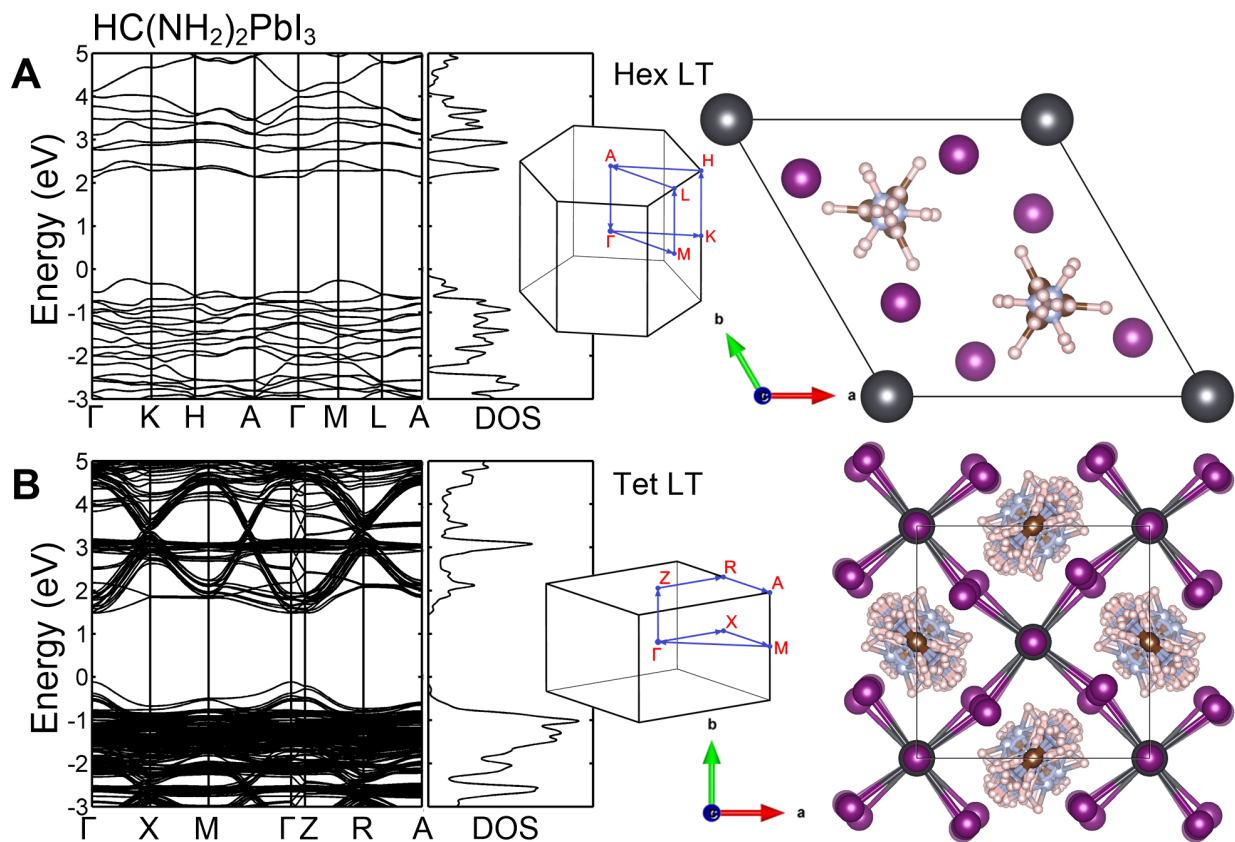**Fig. S8: Electronic band structure of HC(NH₂)₂PbI₃ for the Hex LT and Tet LT phases**. Electronic band structures were obtained by DFT calculations for (*A*) Hex LT and (*B*) Tet LT phases. The crystal structures for Hex IT phases were taken from Ref. (S3), while the crystal structure of the Tet LT phase was determined by Rietveld refinement of neutron diffraction and synchrotron x-ray data taken at 100 K. Here all the crystallographically equivalent positions of the FA⁺ molecule are shown. The geometry of a single FA⁺ molecule is shown in the inset of Fig. 5*F*.

Fig. S9
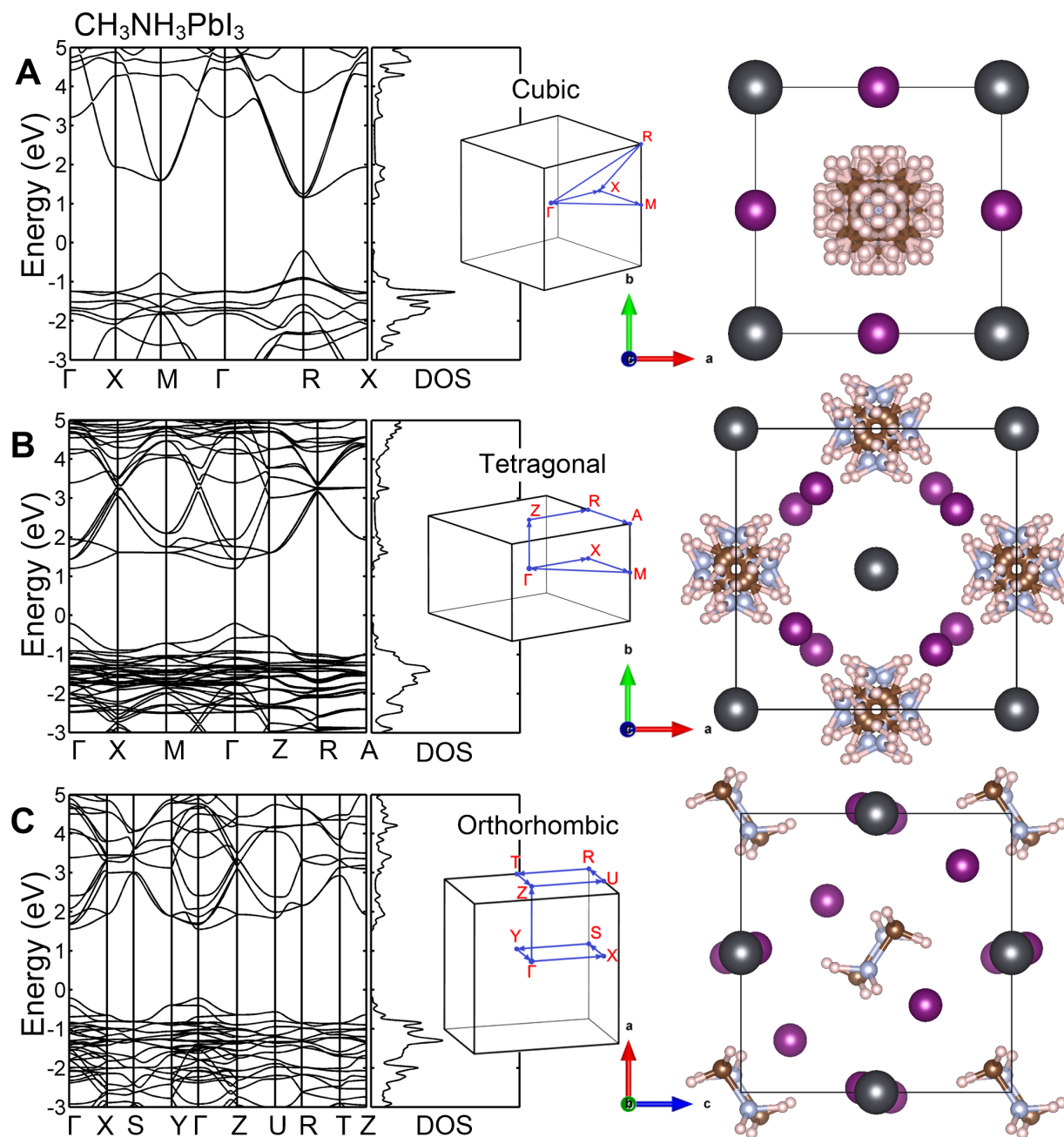
Fig. S9: Electronic band structure of CH₃NH₃PbI₃. Electronic band structures were obtained by DFT calculations for (*A*) cubic, (*B*) tetragonal and (*C*) orthorhombic phases of CH₃NH₃PbI₃. The crystal structures used were from previous neutron and x-ray diffraction studies (S8, S9).
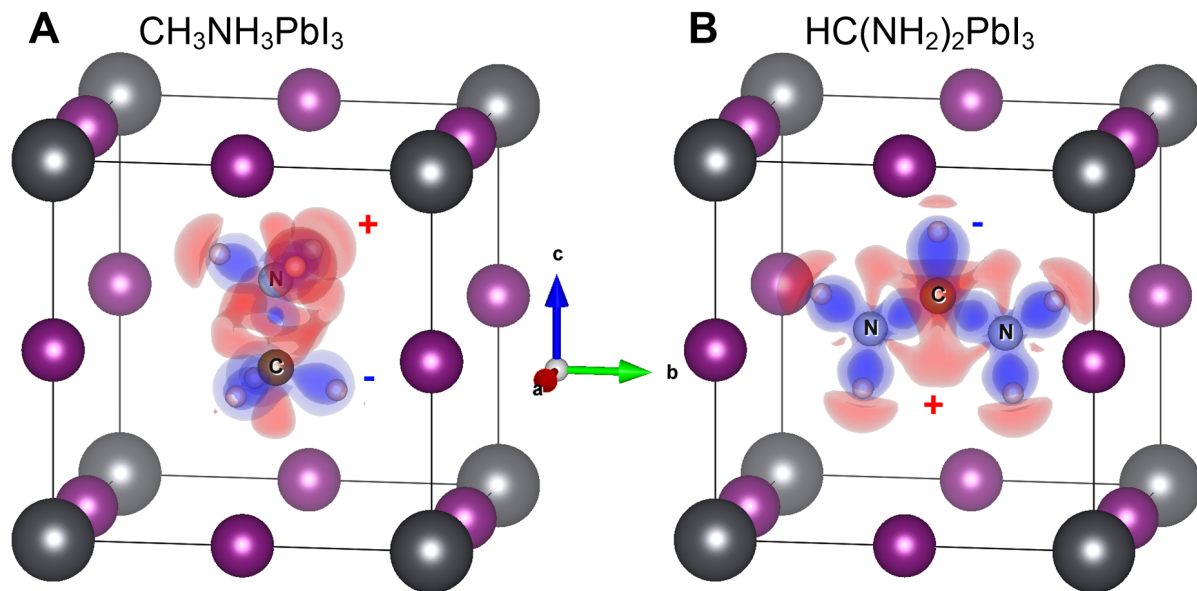
A CH$_3$NH$_3$PbI$_3$

B HC(NH$_2$)$_2$PbI$_3$

Fig. S10: Electronic charge densities of CH$_3$NH$_3^+$ and HC(NH$_2$)$_2^+$ cations. In order to show clearly the electric polarity in the molecule, the charge density was subtracted from a direct sum of single-atom charge densities of each atom. The blue and red surfaces are isosurfaces of "excessive" electrons and holes, respectively.
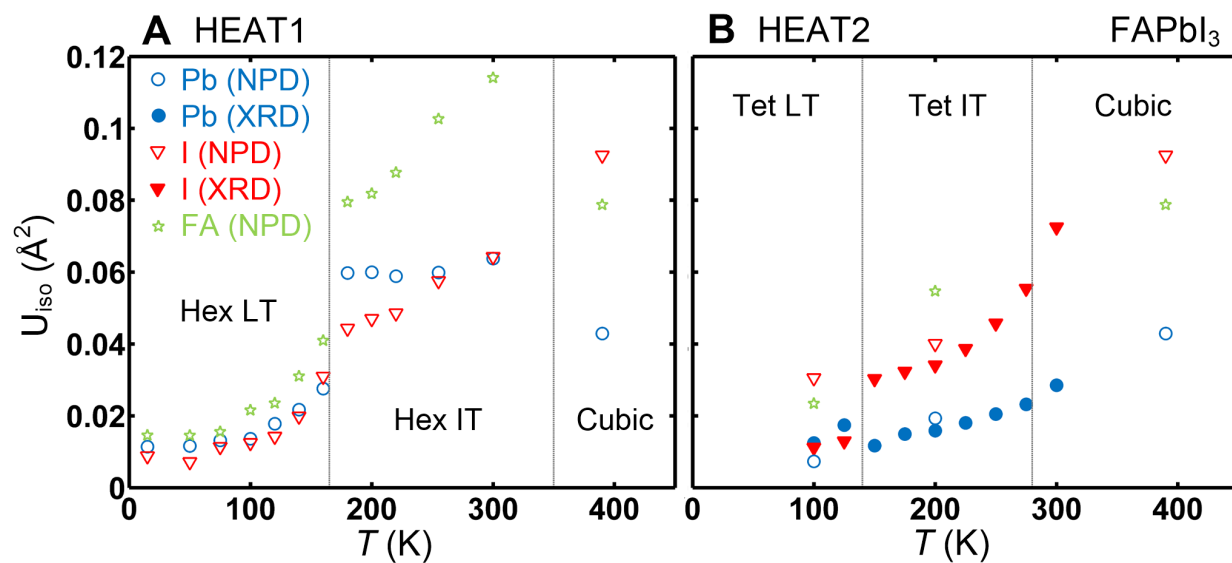
Fig. S11: Isotropic thermal factor of Pb, I and organic cation of FAPbI₃ as a function of temperature. These factors were obtained for (*A*) HEAT1 and (*B*) HEAT2 by Rietveld refinement of synchrotron X-ray (filled symbols) and neutron (open symbols) diffraction data.
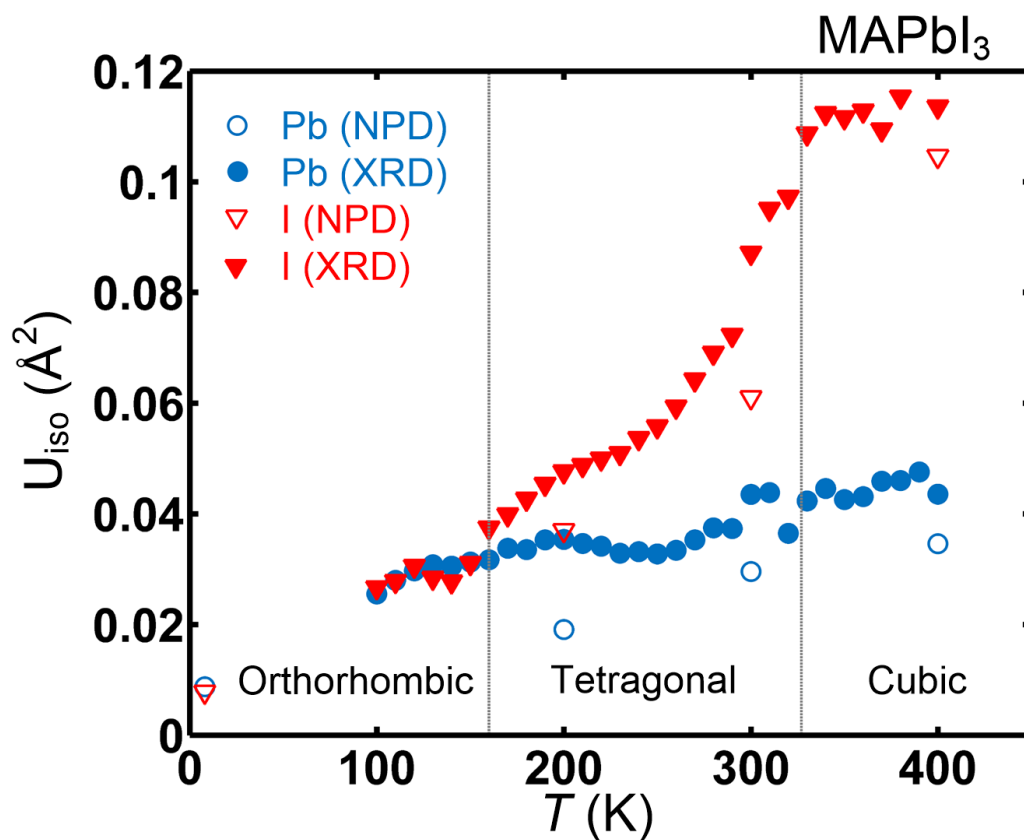
Fig. S12: Isotropic thermal factor of Pb, I and organic cation of MAPbI₃ as a function of temperature. These factors were obtained by Rietveld refinement of synchrotron X-ray (filled symbols) and neutron (open symbols) diffraction data.